

1 Recent advances in experimental design and data analysis to characterize  
2 prokaryotic motility

3

4 <sup>1,2</sup> Megan Marie Dubay, <sup>1</sup>Jacqueline Acres, <sup>3</sup> Max Riekeles, and <sup>1</sup> Jay L. Nadeau\*

5 <sup>1</sup>Department of Physics, Portland State University, 1719 SW 10<sup>th</sup> Ave., Portland, OR 97201

6 <sup>2</sup>Current address: Department of Physics and Astronomy, University of North Carolina, 120 E. Cameron  
7 Ave., Chapel Hill, NC 27514

8 <sup>3</sup>Astrobiology Group, Center of Astronomy and Astrophysics, Technical University Berlin,  
9 Hardenbergstraße 36A, 10623 Berlin, Germany

10

11 \*To whom correspondence should be addressed: Jay Nadeau, SRTC Room 134, Department of Physics,  
12 Portland State University, 1719 SW 10<sup>th</sup> Ave., Portland, OR 97201, nadeau@pdx.edu

13

14

15

## ABSTRACT

16 Bacterial motility plays a key role in important cell processes such as chemotaxis and biofilm  
17 formation, but is challenging to quantify due to the small size of the individual microorganisms  
18 and the complex interplay of biological and physical factors that influence motility phenotypes.  
19 Swimming, the first type of motility described in bacteria, still remains largely unquantified.  
20 Light microscopy has enabled qualitative characterization of swimming patterns seen in different  
21 strains, such as run and tumble, run-reverse-flick, run and slow, stop and coil, and push and pull,  
22 which has allowed for elucidation of the underlying physics. However, quantifying these  
23 behaviors (e.g., identifying run distances and speeds, turn angles and behavior by surfaces or  
24 cell-cell interactions) remains a challenging task. A qualitative and quantitative understanding of  
25 bacterial motility is needed to bridge the gap between experimentation, omics analysis, and  
26 bacterial motility theory. In this review, we discuss the strengths and limitations of how phase  
27 contrast microscopy, fluorescence microscopy, and digital holographic microscopy have been  
28 used to quantify bacterial motility. Approaches to automated software analysis, including cell  
29 recognition, tracking, and track analysis, are also discussed with a view to providing a guide for  
30 experimenters to setting up the appropriate imaging and analysis system for their needs.

31

32 Keywords: Biological Optics; Cell Locomotion; Chemotaxis; Biological Movement

33

34

35

36

37

## 1. INTRODUCTION

38 Since the development of a tracking microscope in 1971(Berg, 1971), researchers have  
39 recognized the need for tools that would allow for both imaging and recording of microbial  
40 motility. The ideal experimental apparatus would record images of cells in a 3D volume with high  
41 signal to noise ratios and at high framerates. This would in turn allow cell tracking algorithms to  
42 easily characterize cell motility quickly and effectively, preferably with minimal user input.  
43 Advances over the past few decades have brought this ideal case closer to reality. Unfortunately,  
44 despite numerous experimental setups and data analysis techniques, the holy grail of precise and  
45 straightforward 3D tracking of bacteria remains elusive. That being said, progress has been made  
46 in understanding motility phenotypes of various bacteria using a variety of imaging and software  
47 techniques, which we will summarize here with the goal of making it easier for those planning  
48 bacterial tracking experiments to choose hardware and software.

49 Acquisition and analysis software may be open-source or commercial. Choices are determined  
50 by the project's budget as well as any needs to re-tune available code to custom optical systems.  
51 The platforms ImageJ (FIJI) (Schindelin et al., 2012) and ICY (de Chaumont et al., 2012) are  
52 highly versatile, open source, and widely used by biologists, so in this review we will mention  
53 when a FIJI or ICY package or plug-in exists for a particular technique. Many packages for  
54 MATLAB are also available, as well as custom programs based in Python.

55 Several recent reviews of cell and particle motility exist, and we will focus on areas  
56 complementary to those recently discussed. One thorough review covers tracking of more complex  
57 cells, which largely applies to 2D processes such as cell migration as well as tracking of sub-  
58 cellular organelles, and offers a comprehensive list of software for this application (Emami et al.,  
59 2021). While there is significant overlap with bacterial tracking, the latter presents certain specific

challenges, particularly fast speeds and 3D motion. It is also simpler in some respects, since contouring is usually not necessary and subcellular features are neglected. Another recent review focuses on amoeboid motility to illustrate the steps required in motility quantification of complex cells (Boquet-Pujadas et al., 2021). Single-molecule investigations of bacterial cells using high resolution fluorescence techniques have been also well reviewed elsewhere (Gahlmann and Moerner, 2014). Additionally, “microswimmers” may also refer to non-living particles. Many studies have been conducted on microspheres (Lee et al., 2007, Lei et al., 2015, Zhang et al., 2017) and other types of nonliving swimmers, and approaches to their tracking have been reviewed (Pané et al., 2019). Although nonliving particles can be used to approximate bacteria in size, their lack of self-motility and relatively slow speeds simplify data processing in ways that are not possible for bacteria; in addition, they may be engineered to provide contrast for different imaging techniques. We will limit the scope of the current review to tracking of unstained, self-motile microorganisms on the order of 1-2  $\mu\text{m}$  in diameter and the unique challenges these present, specifically complex, frequently overlapping tracks and speeds of up to hundreds of cell lengths per second.

### 1.1. Bacterial motility

77 Motility is a crucial microbial phenotype that has evolved independently in Bacteria, Eukarya,  
78 and Archaea. On the molecular level, 18 different motility types can currently be identified, with  
79 more undoubtedly to be discovered in microorganisms that have not yet been cultured (Miyata et  
80 al., 2020). Some bacteria use flagella for swimming motility, whereas archaea use the unrelated  
81 archaellum (Albers et al., 2018, Albers and Jarrell, 2015). Directional motion allows  
82 microorganisms to find nutrients, escape predators, waste products, and toxins, and assemble into  
83 biofilms. The best studied microorganisms are *Escherichia coli* (*E. coli*) and *Salmonella enterica*

84 serovar Typhimurium, and much of what we know about motility and chemotaxis come from these  
85 organisms (Bardy et al., 2017).

86  
87 Research into different microorganisms with different motility patterns has grown over the past  
88 two decades, identifying new classes of motility, motility in new classes of microorganisms, and  
89 elucidating the physics of swimming at the micron scale. Flagellins are highly conserved in  
90 bacteria, but flagellar conformations of bacteria and archaea vary greatly, as do body shapes, as  
91 shown in Fig. 1 (a), (b). At least six types of swimming patterns can be distinguished in low-  
92 resolution microscopic recordings; these correspond to both flagellar arrangement and function.  
93 The common gut and soil bacteria *Escherichia coli* and *Bacillus subtilis* have peritrichous flagella  
94 and show a well-characterized pattern of motility involving “runs” (where all the flagella rotate  
95 together in a bundle, turning counter-clockwise) and “tumbles” (where the flagella turn clockwise  
96 and the bundle separates) (Fig. 1 (c)). Bacteria with peritrichous flagella that only rotate clockwise  
97 can show run-and-stop or run-and-slow patterns (Armitage and Schmitt, 1997) (Fig. 1 (d)).  
98 Another pattern, the “run-reverse flick” pattern of aquatic microorganisms with a single polar  
99 flagellum, such as *Vibrio alginolyticus*, is also known (Fig. 1 (e)) (Stocker, 2011). This pattern of  
100 swimming, common in marine bacteria, involves 180-degree reversals, creating zig-zag tracks,  
101 often at high speeds compared to bacteria with peritrichous flagella (up to 100  $\mu\text{m/s}$  vs. 10-30  
102  $\mu\text{m/s}$ ). Another type of swimming seen with a single flagellum is the stop-and-coil motion of  
103 microorganisms such as *Rhodobacter sphaeroides*, where the flagellum cannot reverse direction,  
104 so it coils in order to allow the microorganism to change orientation (Armitage, 1999) (Fig. 1 (f)).  
105 Motile magnetotactic cocci have been identified that have peritrichous flagella and swim in a  
106 helical motion due to push-pull action of the flagella (Zhang et al., 2014) (Bente et al., 2020) (Fig.  
107 1 (g)). Swimming patterns of spiral-shaped cells are characterized more by the appearance of the

108 cells themselves rather than the track of movement. In Spirochetes such as *Borrelia* and  
109 *Treponema*, pairs of flagella rotate within the periplasm, generating a helical wave (Tahara et al.,  
110 2018). In spirochaetes, two “run” modes and two non-translational modes have been identified. In  
111 general, changes in flagellar number, arrangement, hook length, or other parameters profoundly  
112 (Zhu et al., 2022) affect motility and chemotaxis patterns (Najafi et al., 2018).

113 Other types of swimming continue to be elucidated. *Synechococcus* is a cyanobacterium that  
114 swims without flagella (Waterbury et al., 1985). Other types of non-swimming motility are also  
115 seen but are less understood. Type IV pili are used by many species for motility on surfaces,  
116 usually called twitching motility (Piepenbrink et al., 2016). Gliding refers to a surface mechanism  
117 used by a heterogeneous group of bacteria, powered by ion channels and secretory mechanisms  
118 independent of flagella (Nan and Zusman, 2016). Sliding is a type of surface motility that requires  
119 no active motor (Holscher, 2017). Staphylococci, previously considered non-motile, have been  
120 shown to have means of locomotion that include spreading, darting, and comet formation (Pollitt  
121 and Diggle, 2017). In this review we focus on motility that is tracked in liquid medium, thus  
122 restricting our discussion to swimming and to some extent gliding.

123 Much less is known about swimming in archaea, although it has been known for some time that  
124 swimming is induced by rotation of the archaellum. Much of the difficulty in studying these  
125 microorganisms arises from the need to observe them under extremophilic conditions: anaerobic,  
126 temperature extremes, and/or very high salt. A systematic study of the swimming patterns of  
127 several types of archaea was performed in 2012 (Herzog and Wirth, 2012). Some archaea show  
128 the fastest movement relative to body size of any known organism on Earth. The patterns of fast-  
129 swimming archaea were characterized as “run and seek,” with different behaviors (slower zig-  
130 zagging) near the surface of the slide. The tracks are closest to the bacterial “run and flick” pattern,

131 but many archaea are distinguished by their remarkable speeds. Some microscopy systems  
132 designed to accommodate the needs of archaea will be specifically mentioned in this paper.

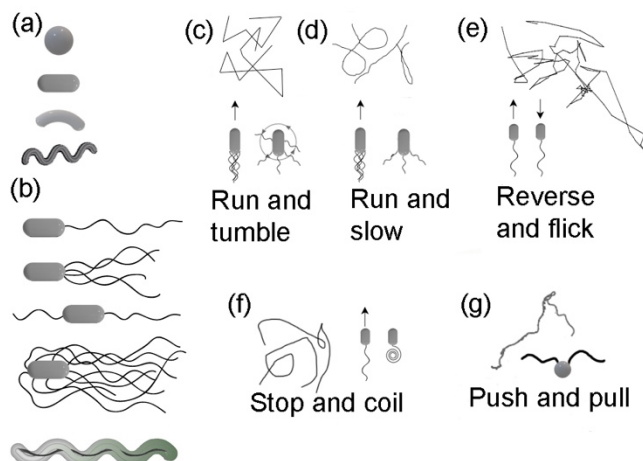
133 High-resolution recordings permit observation of detailed features of tracks rather than  
134 characterizing all forward motion as simply “runs.” These studies have led to an increasing  
135 appreciation of the importance of cell body shape in swimming. The cell body is often considered  
136 to be a source of passive drag, but non-rod-shaped cell bodies may contribute to motility. Many  
137 marine motile bacteria are curved rods falling within a relatively narrow range of elongation and  
138 curvature. Detailed models of swimming speeds and chemotaxis efficiencies have identified  
139 shapes that are optimized across a panel of selective parameters (Schuech et al., 2019). Even more  
140 recently, helical motion of a crescent-shaped bacterial cell, *Caulobacter crescentus*, was observed  
141 to affect swimming patterns in this singly flagellated cell (Yuan et al., 2021).

## 1.2. Imaging challenges

144 Understanding motility phenotypes provides a framework of what quantities might be of  
145 interest to characterize and quantify bacterial motility. For instance, the length of a bacterium's  
146 "run" could change based on environmental factors such as viscosity. Rapid characterization of  
147 run length for numerous cells would give good statistics and provide a sound basis of comparison.  
148 However, quantification of bacterial motility remains challenging due to the technological  
149 difficulty of imaging live, active microorganisms on the order of the size of  $2\lambda$  of visible light that  
150 can move tens or even hundreds of cell lengths per second. For any imaging system, a variety of  
151 trade-offs must be made according to the specific goals of the experiment. Increased spatial  
152 resolution usually leads to decreased field of view, unless cameras with very high sensor sizes are  
153 used. High frame rates are necessary to capture fast processes but lead to extremely large datasets  
154 if carried out over long times. Fluorescent labels increase signal to noise of imaging, but dyes may

155 affect microorganism behavior. Finally, data may be analyzed cell by cell, which optimizes  
156 accuracy but limits the number of cells considered; or statistical analyses may treat hundreds to  
157 thousands of cells at a time but fall prey to false positive and false negative identification of tracks.

158 The purpose of this review is to identify the recent breakthroughs in bacterial motility analysis  
159 and identify what parameters of an imaging system are necessary to study the identified  
160 phenomena and what the limiting technological factors are in each case. Summary tables are  
161 provided that should assist researchers in choosing imaging and tracking techniques that are  
162 appropriate for the systems studied, or in developing custom systems that can push the limits of  
163 what is currently known. Both hardware and software are considered, with particular attention to  
164 automated identification and tracking algorithms.



165  
166 FIG. 1. Cell morphologies and swimming patterns. (a) Both bacteria and archaea show a variety of body shapes that  
167 can be classified as cocci (spherical), bacilli (rods), curved rods, or spirals. (b) Flagella and archaella may be  
168 attached to the cell in a variety of patterns. A rod-shaped body is shown for simplicity, but the different flagellar  
169 patterns are seen across body types. From top to bottom are monotrichous (a single flagellum, which may be lateral  
170 or polar), lophotrichous (multiple flagella attached at a single point), amphitrichous (flagella on each end),  
171 peritrichous (multiple flagella attached at different points all over the surface), and periplasmic (flagella enclosed in  
172 the periplasmic space). (c) Run-and tumble pattern as exemplified by *E. coli*. (d) Run-and slow pattern as  
173 exemplified by *Sinorhizobium melioli*. (e) Reverse and flick as exemplified by *V. alginolyticus*. (f) Stop and coil as  
174 exemplified by *R. sphaeroides*. (g) Push and pull as identified by the eukaryote *Chlamydomonas*.  
175

176

## 2. MICROSCOPY TECHNIQUES

177     Throughout the years, a variety of imaging techniques have been employed with the goal of  
178     bacterial tracking. These include phase contrast microscopy, darkfield microscopy, fluorescence  
179     microscopy, and digital holographic microscopy (both in-line and off-axis). Each system has  
180     tradeoffs; the most commonly used in recent studies are discussed in detail below.

181

### 182                   2.1. Phase contrast microscopy

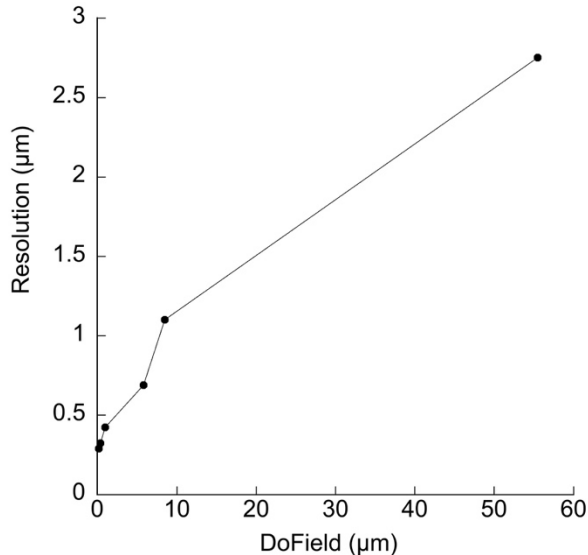
183     Phase contrast microscopy is a standard technique found in most microbiology laboratories and  
184     easily implemented on all commercial microscopes. Depending upon the objective lens chosen, it  
185     is capable of either high resolution or fairly large depth of field. Diffraction-limited lateral (XY)  
186     resolution is given by  $\lambda/NA$ , where  $\lambda$  is the wavelength of illuminating light and  $NA$  is the  
187     numerical aperture of the objective. Depth of field  $d$  is the sum of two terms, a wave term and a  
188     geometrical optical term (Davidson and Spring):

189

$$190 \quad d = \frac{n\lambda}{(NA)^2} + \frac{ne}{M(NA)}, \quad (1)$$

191

192     where  $n$  is index of refraction of the medium between the lens and the coverslip (air or  
193     immersion oil),  $e$  is the smallest resolvable element, and  $M$  is the magnification. (Fig. 2).



194  
 195 FIG 2. Tradeoff between resolution and depth of field for 550 nm illumination and air objectives. The non-linear  
 196 relationship can be appreciated by observing that for bacterial cells on the order of 1  $\mu\text{m}$ , the ability to resolve the  
 197 cells will lead to a depth of field of  $< 10 \mu\text{m}$ , whereas a decrease of resolution for 2.5  $\mu\text{m}$  will permit a depth of field  
 198 of  $> 50 \mu\text{m}$ .  
 199

200 Phase contrast microscopy represents one of the most established and successful methods of  
 201 bacterial tracking. It has been used for some significant recent results, such as tracking a variety  
 202 of swimming archaea, including hyperthermophiles (Herzog and Wirth, 2012) and discovery of  
 203 the importance of cell body motion in swimming of *Caulobacter* (Liu et al., 2014).

204 The primary disadvantage of phase contrast microscopy is that cells are lost as they swim in X  
 205 and Y, or out of focus in the Z plane. Manual manipulation or digital tracking stages may be used  
 206 to follow cells. Methods to follow single cells include the use of scanning stages (Berg and Brown,  
 207 1974, Frymier et al., 1995, Yang et al., 2015) or scanning objectives (Corkidi et al., 2008). These  
 208 methods are limited by their scanning speed. Most recently, a technique has been proposed for  
 209 determining Z depth in out-of-focus microorganisms by fitting the Airy ring pattern to calibrated  
 210 patterns from test cells (Taute et al., 2015).

211 In some experiments, it is not necessary to permit the cells to swim freely in Z. In this case,  
 212 sample chambers or flow cells may be constructed that restrict the cells to a single focal plane.  
 213 This is useful when only 2D motion is necessary, such as to determine the fraction of motile cells

214 or a general idea of the swimming speed. This may be useful for determining cell health or growth  
215 phase (Ziegler et al., 2015).

216 The typical light microscopes used for phase contrast (or related techniques such as differential  
217 interference contrast [DIC]) may be modified for use with extremophiles. The low-temperature  
218 swimming record seen in the bacterium *Colwellia psychrerythraea*, -15 °C, was determined using a  
219 laboratory microscope customized by the vendor for use at subzero temperatures. The entire  
220 instrument and its operator were then located in an adjustable-temperature cold room (Junge et al.,  
221 2003). At the other extreme, a heated indium tin oxide (ITO) chamber heated to 75 °C, with the  
222 microscope objectives heated to 65 °C, was used for imaging hyperthermophilic archaea (Charles-  
223 Orszag et al., 2021).

## 2.2. Digital holographic microscopy

Digital holographic microscopy (DHM) is a volumetric technique based upon interferometry, where a volume of view is captured in a single snapshot (hologram). The hologram appears as a pattern of Airy rings indicating out-of-focus objects throughout the focal depth. The typical approach to analyzing DHM data is to reconstruct the optical field through a chosen Z depth and spacing based upon the hologram. Reconstruction methods depend upon the DHM geometry used, namely “off-axis”, where object and reference beams interfere at an angle (Fig. 3 (a)), or “inline” imaging (DIHM) where a single beam serves as both object and reference (Fig. 3 (b)). The different approaches to geometry and reconstruction have been reviewed in (Xiao et al., 2014) and (Myung, 2010).

234 Off-axis holography separates the spatial frequencies from the unscattered “direct term” as well  
235 as separating the real and virtual images from one another, facilitating ease of reconstruction into  
236 both amplitude and quantitative phase images (Schnars and Jüptner, 2002). Amplitude images are

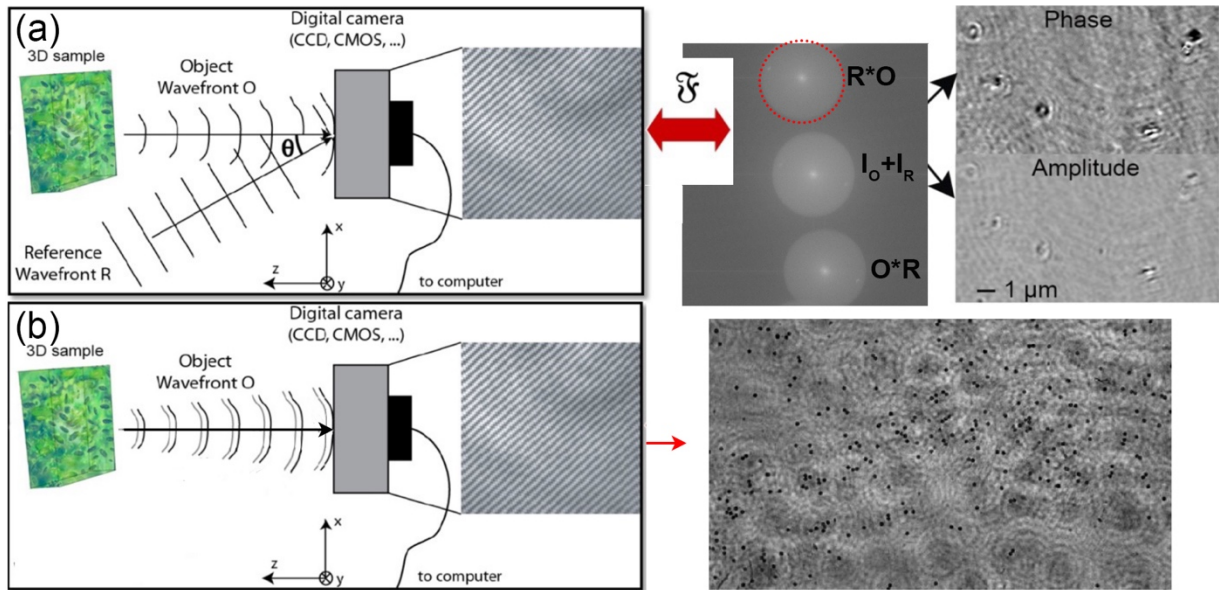
237 equivalent to transmission light microscopy. Quantitative phase images have no direct counterpart  
238 in ordinary light microscopy and are related to the product of the cell thickness  $h$  and the difference  
239 in refractive index between the medium ( $n_m$ ) and cell ( $n_c$ ), with the phase shift  $\Delta\phi$  given by  
240 (Marquet et al., 2005, Rappaz et al., 2005) (Marquet, Rappaz, Magistretti, Cuche, Emery, Colomb  
241 and Depeursinge, 2005)

242 
$$\Delta\phi = \frac{2\pi}{\lambda} h(n_c - n_m) \quad (2),$$

243 where  $\lambda$  is the wavelength of illumination. This value is modulo  $2\pi$ , so complications arise  
244 when  $\Delta\phi$  exceeds  $2\pi$ . However, for experiments involving bacteria, this is rarely an issue. Instead,  
245 the challenge lies in resolving any phase shift, as  $n_c - n_m$  is on the order of 0.03-0.05 (Wyatt,  
246 1970), and methods such as frame averaging to reduce noise cannot be performed on rapidly  
247 moving cells.

248 The lateral resolution of DHM is equivalent to that of brightfield microscopy. Reconstruction  
249 of DIHM images is more complicated, since the direct term is not readily filtered out, leading to  
250 “ghost” images. Nonetheless, many algorithms have been developed for reconstruction and phase  
251 retrieval from these images (Galande et al., 2021, Latychevskaia and Fink, 2009, Micó et al., 2011,  
252 Wang et al., 2018, Zhang et al., 2003).

253



254 FIG. 3. Off-axis DHM and DIHM. (a) Off-axis holography uses the interference of two coherent beams of light from  
 255 a single source to record the complete sample volume in each captured frame. The “object” beam passes through the  
 256 sample, while the “reference” beam takes an identical-length unperturbed path to the detector. The two beams are  
 257 interfered at the detector array and the resulting interference pattern records a pattern of interference fringes which,  
 258 in Fourier space, yield the real image ( $O^*R$ ), the virtual image ( $R^*O$ ), and the so-called “direct” term  $I_o + I_R$ . Either  
 259 the real or virtual image is selected in Fourier space (as indicated by the red circle) and reconstructed using a chosen  
 260 algorithm; numerical refocusing allows reconstruction of phase and amplitude images through the depth of the  
 261 sample. (b) Digital in-line holographic microscopy (DIHM) uses a single beam which is assumed to be slightly  
 262 perturbed by the object and interferes with itself. The resulting hologram does not capture information as fringes.  
 263 The illustrated reconstruction method shows a dark-field-like reconstruction that works for phase, amplitude, and  
 264 phase-amplitude objects (hologram and reconstruction are adapted from  
 265 (<https://www.sciencedirect.com/science/article/pii/S0143816620300762>) under terms of the Creative Commons  
 266 license; the images were cropped).

267

268 The limit to the depth that can be reconstructed from DHM results from a degradation of spatial  
 269 resolution as the reconstruction propagator extends outside the focal plane. For typical bacterial  
 270 imaging experiments with  $\sim 1 \mu\text{m}$  spatial resolution, the depth of the sample is limited to  $\sim 1 \text{ mm}$   
 271 (Kühn et al., 2014), which is very large compared with other microscopic techniques and which  
 272 represents the biggest advantage of this imaging technique, allowing a simultaneous snapshot of  
 273 essentially an unconstrained volume. Acquisition rates are limited by the camera frame rate. As a  
 274 result of this major advantage, a large number of recent papers have reported prokaryotic tracking  
 275 using DHM. The optics of DHM are also simple and the hardware is low in cost.

276 The disadvantage of DHM is a generally low resolution (Peng and Caojin, 2022), and the  
277 intrinsic low contrast of most prokaryotic cells in amplitude and phase. Some dyes may increase  
278 contrast for DHM, but this is an area that has not been well explored (Nadeau et al., 2016). The  
279 development of agents for specific enhancement of phase contrast has also been little studied,  
280 though it is possible through labeling techniques such as genetically encoded air-filled vesicles  
281 which provide substantial change in refractive index relative to aqueous medium (Farhadi et al.,  
282 2020).

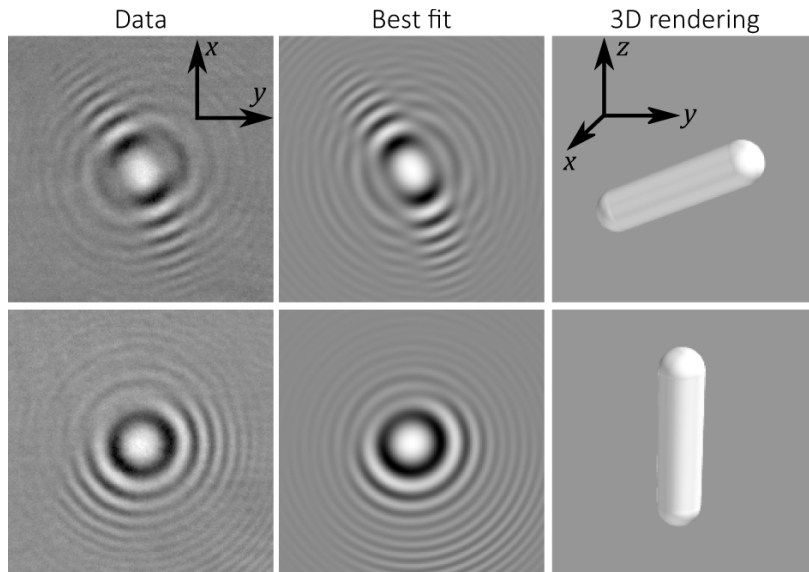
283 DHM leads to large datasets and its analysis is computationally intensive. A 30 second dataset  
284 at 15 frames/s and 4 Mpx yields 1.8 GB of images before reconstruction. Depending upon the z-  
285 spacing selected for reconstruction, a full reconstructed dataset may be upwards of 1 Tb. Few  
286 software packages are available for analysis. Commercial software is usually tied to a specific  
287 instrument. Open-source Fiji for both in-line and off-axis DHM have recently been reported  
288 (Buitrago-Duque and Garcia-Sucerquia, 2022) (Cohoe et al., 2019).

289 An alternative to reconstruction is to extract Z information directly from the holograms. If the  
290 form of the diffraction pattern or the Z-position of the object are known, the Airy pattern may be  
291 easily fit to a function based upon Lorenz-Mie theory (Cheong et al., 2009, Lee et al., 2007,  
292 Ruffner et al., 2018). For more complex shapes, a discrete dipole approximation must be used  
293 (Wang et al., 2014). Open-source software is available to perform these fits, but this approach is  
294 highly complex and computationally intensive when neither the exact shape and size nor the axial  
295 depth are known. Good signal to noise is also essential to permit accurate fitting of the patterns.  
296 This approach has been used to track runs and tumbles in *E. coli* (Wang et al., 2016) (Fig. 4).

297 DHM instruments are simple and robust and readily adapted to imaging at cold temperatures.  
298 We have performed in situ recordings at air temperatures down to -13 °C (Lindensmith et al.,

299 2016). For imaging thermophiles, we have created a low-cost system where the microscope is  
300 submerged in a pot of boiling water with the optics protected by a plastic bag. Imaging  
301 temperatures of  $>90$  °C can be obtained using this setup (Dubay et al., 2022).

302 A summary of the hardware and software parameters in recent DHM studies of bacteria is given  
303 in Table I.



304  
305 Fig. 4. Holograms of freely swimming *E. coli* in a time series. Two frames are shown in the left column, where the  
306 asymmetry in the fringes is noticeably different between the frames. The best-fit holograms are shown in the middle,  
307 and three-dimensional renderings from the best-fit holograms are shown on the right using the discrete dipole  
308 approximation and the software HoloPy (<http://manoharan.seas.harvard.edu/holopy/>). (Image from: Anna Wang,  
309 Rees F. Garmann, Vinodhan N. Manoharan, “Tracking runs and tumbles with scattering solutions and digital  
310 holographic microscopy,” Opt. Express 24, 23719-23725 (2016); © 2016 Optica Publishing Group under the terms  
311 of the Open Access license. Image not edited).  
312

Microorganism Studied	Software	Objective(s)	$\lambda$ (nm)	Camera
<i>E. coli</i> <sup>a</sup>	HoloPy	60x NA=1.2 In-line	660	Photon Focus MVD-1024E- 160, 100fps
<i>E. coli</i> <sup>b</sup>	Trajectories linked by home-made Python code	40x NA=0.6 In-line	455	sCMOS 20Hz for 2min
<i>S. marcescens</i> <sup>c</sup>	Manual Tracking / 2D WTMM segmentation method	NA=0.3 Off-axis	405	170ms intervals for 3min
<i>E. coli</i> <sup>d</sup>	No tracking	40x NA=0.6 100x NA=1.4 In-line	455 450	sCMOS
<i>E. coli</i> <i>Pseudomonas</i> <sup>e</sup>	Coordinates from Rayleigh-Sommerfeld propagation/Trajectories from homemade program	40x NA=0.6 In-line	455	sCMOS 20fps
<i>P. aeruginosa</i> <sup>f</sup>	Bacterial trajectory: bespoke Matlab scripts: DHMTracking and StackMaster	60x NA=1.4 In-line	685	CMOS 41.6Hz
<i>E. coli</i> <sup>g</sup>	Image recognition 3D tracking method	40x NA=0.6 In-line	505	sCMOS 50fps/2min
<i>E. coli</i> <sup>h</sup>	Median division followed by reconstruction; projection and tracking in XY and manual extraction of Z	20x NA=0.5	515 642	Mikrotron MC-1362 CMOS 50 fps
<i>Pseudomonas aeruginosa</i> <sup>i</sup>	Median subtraction; reconstruction and projection into XY, XZ, and YZ; polynomial regression smoothing	20x NA 0.4 In-line	532	pco.imaging CMOS 5 fps
<i>B. subtilis</i> <sup>j</sup>	Custom open source reconstruction and tracking software	NA 0.3 aspheres	405	Allied Prosilica GT 15 fps

314 Table I. Imaging parameters in recent bacterial motility studies using holographic microscopy.

315 <sup>a</sup> Wang et al. Optics Express 2016, 24, (21), 23719-23725.316 <sup>b</sup> Qi et al. Langmuir 2017, 33, (14), 3525-3533.317 <sup>c</sup> Marin et al. Methods 2018, 136, 60-65.318 <sup>d</sup> Huang et al. Optics Express 2018, 26, (8), 9920-9930.319 <sup>e</sup> Peng et al. Langmuir 2019, 35, (37), 12257-12263.320 <sup>f</sup> Hook, et al. Msystems 2019, 4, (5).321 <sup>g</sup> Wang et al. Optics Express 2020, 28, (19), 28060-28071.322 <sup>h</sup> Farthing et al. Optics Express 2017, 25, (23), 28489-28500.323 <sup>i</sup> Vater et al. PLoS One 2014, 9, (1), e87765.324 <sup>j</sup> Dubay et al. Frontiers in Microbiology 2022 <https://doi.org/10.3389/fmicb.2022.836808>

325

326

### 2.3. Fluorescence microscopy

327

Fluorescence microscopy has the highest signal-to-noise of any of the discussed microscopic techniques. It has a higher effective resolution than other techniques because of reduced noise as well as the ability of targeted probes to highlight small structures, such as flagella, that are ordinarily below the diffraction limit. What we mean by “effective resolution” is that the centroid of a high signal-to-noise image can be localized to nanometer precision even if the object’s size appears inaccurate. This phenomenon has been used to image individual fluorescent nanoparticles  $<5$  nm in diameter as well as to develop superresolution techniques such as PALM and STORM, where centroids of different objects are separated temporally (Waters and Wittmann, 2014).

335

While some dyes might affect motility (Martin and Logsdon, 1987, Wainwright et al., 1997), the advantages of fluorescence make it essential whenever high resolution or high signal-to-noise are needed. Membrane dyes have been shown to have less effect on motility and cell division than DNA-targeting dyes (Charles-Orszag, Lord and Mullins, 2021). When studying extremophiles, it is important to note that many commonly used dyes do not fluoresce under extremes of temperature, salt concentration, and/or pH, and that cell-wall or membrane-targeting dyes that work in bacteria may not work in archaea. Fluorescent probes that work in thermophiles, halophiles, and at pH extremes have been reported (Leuko et al., 2004) (Rastadter et al., 2022) (Maslov et al., 2018).

344

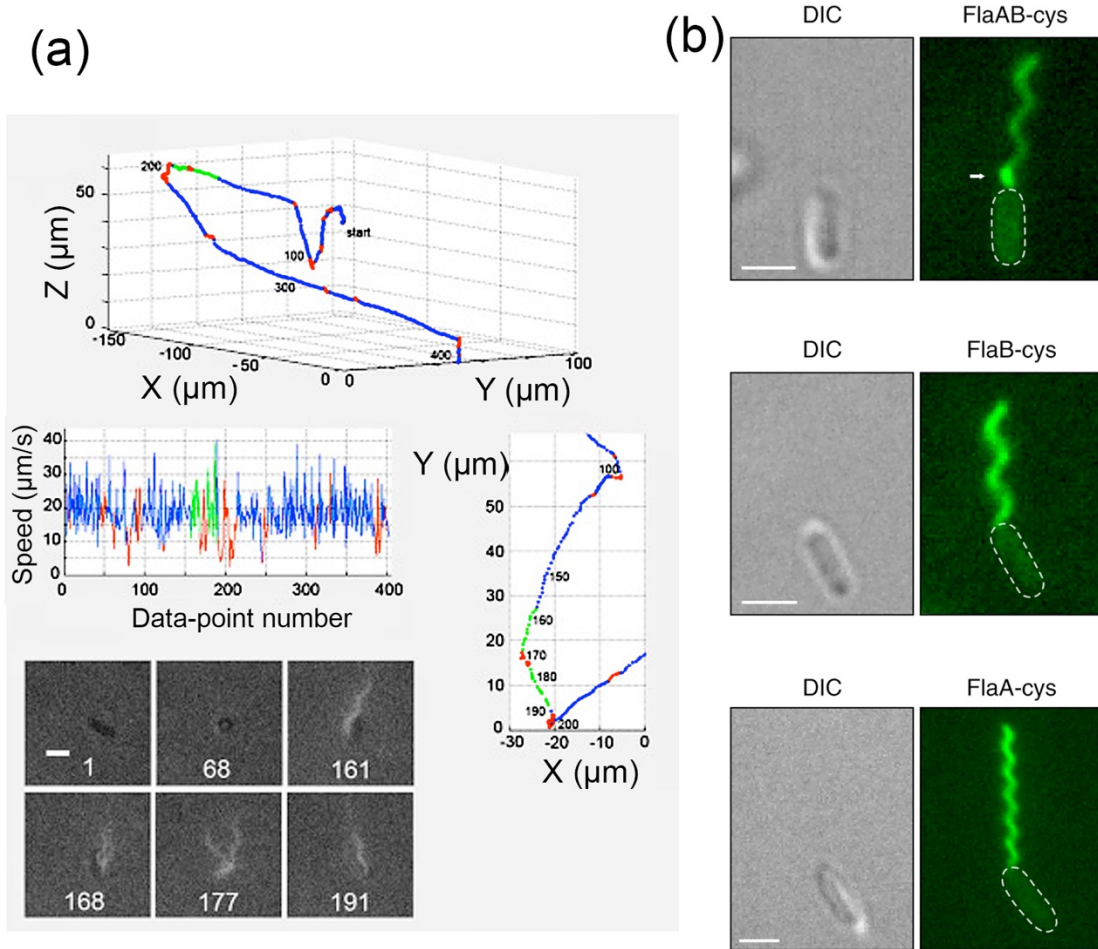
At the whole-cell level, the ability to genetically modify bacteria to express fluorescent proteins (FPs) such as green fluorescent protein (GFP) and its variants has enabled numerous tracking experiments in both simple and complex milieux. FPs have little effect on physiology and demonstrate low phototoxicity, permitting them to be used for long-term recordings, although care should be taken to use green light rather than blue or violet for excitation, as the shorter

349 wavelengths affect cell growth (El Najjar et al., 2020). Green excitation corresponds to Yellow  
350 Fluorescent Protein (YFP) emission; YFP is very commonly used in microbial studies. The GFP  
351 family of proteins requires oxygen for maturation and thus cannot be used in anaerobes; a variety  
352 of oxygen-independent alternatives have emerged recently (Chia et al., 2019, Chia et al., 2020, Ko  
353 et al., 2020).

354 For observation of flagella, fluorescence microscopy with labeling is essential. Fluorescence  
355 has been used to observe correlate flagellar movements with tumbles in *E. coli*, *B. subtilis*, and  
356 motile *Enterococcus* (Turner et al., 2016). Cells were labeled with the dye Alexa Fluor 532, and  
357 an overlay of phase contrast and fluorescence was used to visualize the cell bodies and flagella  
358 (Fig. 5 (a)). Fluorescent labeling of flagella may also be used to provide complementary  
359 information for cells tracked by other means. One study examining the distribution of flagellar  
360 filaments FlaA and FlaB used fluorescent labeling of inserted cysteine residues to visualize the  
361 flagella in individual cells, then used DHM without labeling for high-throughput tracking (Fig. 5  
362 (b)) (Kuhn et al., 2018).

363 The biggest drawback for long-term fluorescence microscopy is photobleaching.  
364 Photobleaching may be reduced by limiting light intensity and/or exposure times or by the addition  
365 of antioxidants to the medium (or the removal of oxygen if possible) (Bernas et al., 2004, Boudreau  
366 et al., 2016, Giloh and Sedat, 1982).

367



368  
 369 Fig. 5. Use of fluorescence microscopy and flagellar labeling to elucidate the role of flagella in swimming. (a) Track  
 370 of a typical untreated *E. coli* cell (upper panel) with combined phase-contrast and fluorescence images (dark and  
 371 light, respectively, lower-left panel). Runs are shown in blue, tumbles are in red, and runs with the laser on are in  
 372 green. Each data point along the trajectory corresponds to one video frame (30/s). At the start, image 1 (lower-left  
 373 panel), the phase-contrast image shows the cell moving parallel to the X-Y image plane. Cell-body measurements  
 374 were made from this image. At image 68, the cell is seen end-on while moving along the Z axis at track point 68.  
 375 The overview (right panel) shows the track in the X-Y plane from points 100–200, and includes laser illumination  
 376 points 157–191. The cell was running with a tight bundle in image 161. A tumble occurred during points 168–177.  
 377 In image 177, as the tumble ended, the bundle started to reform, a process that was completed at point 188 (not  
 378 shown). A tightly formed bundle is evident in image 191. After this point, another tumble began. The scale bar is 2  
 379 μm (From Biophys J. 2016 Aug 9; 111(3): 630–639. doi: 10.1016/j.bpj.2016.05.053, © 2016 Biophysical Society,  
 380 used with permission). (b) Micrographs of cells with fluorescently labeled flagellar filaments displaying the outcome  
 381 of the genetic editing of the flagellin genes (from Kuhn et al, 2018, under terms of the Creative Commons license).  
 382

383 Parameters of recent bacterial tracking studies using fluorescence microscopy are  
 384 summarized in Table II.

385  
 386

Microorganism Studied	Objective(s)	Fluorophore	Camera	Tracking Method
<i>E. coli</i> <sup>a</sup>	100x/ NA 0.9	Yellow fluorescent protein YFP	ANDOR iXon 897 EMCCD (30 fps at 512x512)	Lagrangian tracker (motorized stage, photobleaching correction)
<i>E. coli</i> <sup>b</sup>	60x/NA 1.27	Red fluorescent protein mRFP1	Hamamatsu Orca Flash 4.0 (50 fps)	Custom software, confined channels
<i>E. coli</i> <i>P. aeruginosa</i> <sup>c</sup>	40x, NA 1.0	Vybrant Dyecycle Green	Zeiss, 80 ms exposure	Segmentation and LAP tracking
<i>E. coli</i> <i>B. subtilis</i> <i>Enterococcus</i> <sup>d</sup>	25x LWD/ NA 1.1	Alexa Fluor 532 maleimide (flagellar labeling)	KPC-650BH (30 fps)	Tracking microscope

387 Table II. Parameters used in some recent bacterial tracking studies using fluorescence microscopy.

388 <sup>a</sup> Figueroa-Morales et al. Physical Review X 2020, 10, (2), 021004.

389 <sup>b</sup> Vizsnyiczai et al Nat Commun 2020, 11, (1), 2340.

390 <sup>c</sup> Khong et al. bioRxiv 2020, 2020.05.03.075507.

391 <sup>d</sup> Turner et al. Biophysical Journal 2016, 111, (3), 630-639.

#### 393 2.4. Differential dynamic microscopy

394 Differential dynamic microscopy (DDM) is a recent method (introduced in 2008 and developed  
 395 for bacteria in 2011-2012 (Martinez et al., 2012, Wilson et al., 2011)) that allows critical motility  
 396 parameters such as velocities and fraction of motile particles to be extracted from recordings with  
 397 low signal to noise ratios. DDM uses successive images to characterize the motility of a population  
 398 by calculating the temporal fluctuations of the number density over different length scales. The  
 399 key parameter is the differential image correlation function (DICF),  $g(q, \tau)$ , which is the modulus  
 400 of the difference of two Fourier-space images over a time step  $\tau$ :

$$401 \quad g(q, \tau) = \langle |I(q, t + \tau) - I(q, t)|^2 \rangle_t. \quad (3)$$

402 The DICF is related to the intermediate scattering function (ISF),  $f(q, \tau)$ , by

$$403 \quad g(q, \tau) = A(q)[1 - f(q, \tau)] + B(q), \quad (4)$$

404 where  $A(q)$  depends on the optics, particle shape, and mutual arrangement, and  $B(q)$  represents  
 405 the camera noise. For a mixed population of motile- and non-motile cells with motile fraction  $\alpha$ ,  
 406 the ISF consists of a part due to Brownian motion, represented by the diffusion coefficient  $D$ , and  
 407 a part due to swimming:

408 
$$f(q, \tau) = (1 - \alpha)e^{-q^2 D \tau} + \alpha e^{-q^2 D t} \int_0^\infty dv P(v) \frac{\sin(qv\tau)}{qv\tau}, \quad (5)$$

409 where  $P(v)$  is the velocity distribution function. The term due to swimming decorrelates much  
410 more quickly than that due to Brownian motion, resulting in a two-phase  $f$  that may be fit to a  
411 multi-parameter function to extract the diffusion coefficient, mean swimming speed, and fraction  
412 swimming. The advantages of this method are rapid, tracking-free determination of these key  
413 motility parameters. The disadvantages are lack of visualization, so that spurious results are  
414 difficult to identify; some comparison with manual tracking is needed. In addition, a form for the  
415 velocity distribution function needs to be specified, so some advance knowledge of swimming  
416 characteristics is needed. The technique also requires a large data volume, approximately 1000  
417 frames at 50 frames/s for cells swimming at typical run-and-tumble speeds (10-50  $\mu\text{m/s}$ ).

418 **3. RECORDING APPARATUS AND SOFTWARE**

419 **3.1. Cameras**

420 Commercially available cameras require trade-offs between field of view and framerate. Until  
421 recently, obtaining full 2048x2048 or even 1024 x 1024 pixel images at >50 frames/s required  
422 highly specialized and costly instrumentation. Although fast cameras are becoming more readily  
423 available, obtaining frame rates >50 fps usually requires some downsampling as well as limiting  
424 any simultaneous data imaging. Cameras for fluorescence represent a special category, as they  
425 must be extremely sensitive and have low background; most are cooled. If specialized wavelengths  
426 such as ultraviolet or infrared are imaged, this imposes additional demands upon the camera.  
427 Because of the complexity of the trade-offs, we have identified the camera model in all of the  
428 studies identified in Tables I and II.

429 The effect of framerate on analysis of bacterial tracks has been discussed in the context of a  
430 velocity jump process model, where identification of re-orientation events is key to accurate

431 parameter estimation. As the sampling rate becomes so slow that multiple re-orientation events  
432 between frames become probable, there is a rapid breakdown in analysis accuracy (Harrison and  
433 Baker, 2018).

434 **3.2. Acquisition software**

435 Acquisition software is dependent on the microscopy technique chosen. For most applications,  
436 the camera software is sufficient; a software development kit (SDK) is usually provided with  
437 camera purchase. Manufacturers often sell software separately, but the cost of the software  
438 sometimes exceeds that of the camera. The open-source package MicroManager (Edelstein et al.,  
439 2010) has been developed to interface with a large number of commercial cameras, microscopes,  
440 and accessories in order to minimize costs associated with software.

441 For specialized techniques such as DHM, software is usually custom. Several research groups,  
442 including our own, have made their DHM software openly available (Fregoso et al., 2020, Zhang  
443 et al., 2015).

444  
445 **4. CELL IDENTIFICATION AND TRACKING**

446 Creating and finding tools for cell tracking is an ongoing area of development. In 2012 a “Cell  
447 Tracking Challenge” was hosted by the IEEE International Symposium on Biomedical Imaging  
448 (ISBI). The results were published in 2014 (Chenouard et al., 2014) with the statement “at present,  
449 there exists no universally best method for particle tracking,” and this is still valid today, nearly a  
450 decade later.

451 Large datasets are generated from imaging and recording samples. One of the primary  
452 challenges for bacterial tracking relates to its low signal to noise ratios. There are a variety of both  
453 in-house and commercially available software packages that attempt to solve this problem.  
454 However, there is currently no “black box” solution that works for any bacterial dataset. Cell

455 tracking in 2D and 3D consists of 1) preprocessing the images, 2) detecting the cells and 3) cell  
456 tracking by linking them correctly in successive video frames. Step 1 is usually semi-automated,  
457 whereas steps 2 and 3 can be done manually or automatically.

458

459

#### 460 4.1. Preprocessing

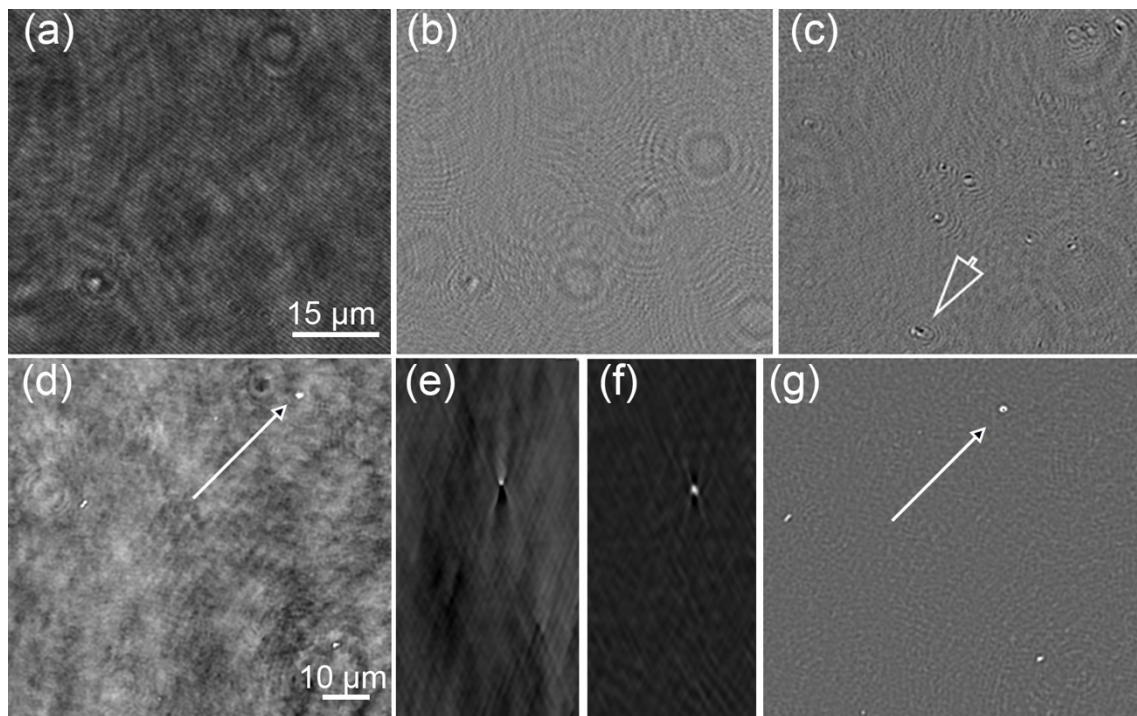
461 The preprocessing necessary is highly dependent upon the technique used. For most brightfield  
462 and phase contrast techniques, some sort of background subtraction using different denoising  
463 approaches (rolling ball algorithm, median, Gaussian filter) is necessary. Such filters are found in  
464 all common image-processing software packages, both open-source and commercial.

465 For DHM, aberration correction is essential. A large amount of research has gone into  
466 development of experimental and software techniques for improvement of DHM contrast. The  
467 denoising approaches to amplitude and phase images are different. While amplitude images are  
468 generally noisier than phase images, especially with respect to speckle noise, approaches to de-  
469 noising are simpler. If the fringes are temporally stable, the hologram may be median subtracted  
470 before reconstruction in amplitude (Bedrossian et al., 2020) (Fig. 6 (a)-(c)). Alternatively,  
471 amplitude images may be median subtracted plane-by-plane after reconstruction. For motile  
472 objects, this usually results in sufficient de-noising for particle detection. Additional signal-to-  
473 noise may be obtained using frame-to-frame subtraction, a method which is frequently used for  
474 DIHM. These techniques remove motionless objects, which can be an advantage or a disadvantage  
475 depending upon the experiment.

476 Quantitative phase retrieval presents specific challenges; approaches to phase aberration  
477 correction have been recently reviewed (Sirico et al., 2022). Digital aberration correction is usually  
478 performed using a reference hologram (Colomb et al., 2006), but this reference must be chosen

479 carefully. If objects are moving, a good reference hologram may be the median of the entire image  
480 stack, provided that the fringes are stable (Fig. 6 (d)). For long acquisitions or when fringes are  
481 not stable, a “rolling mean” of a selected number of images may serve as a reference hologram.  
482 Obtaining an empty reference from a chamber without cells is usually not possible, since many of  
483 the aberrations arise from the precise sample chamber and area of the chamber being imaged. Thus,  
484 even microscopic changes in the slide position can alter the aberrations.

485 An advantage of phase reconstructions is the Gouy phase anomaly, where an object switches  
486 from light to dark across the focal plane (Fig. 6 (e)). This means that the Z-derivative has a  
487 maximum at that point, so the axial derivative of a phase reconstruction reduces noise in Z (Fig. 6  
488 (f)) and in XY (Fig. 6 (g)). The choice of reconstruction spacing for the derivative depends upon  
489 the dataset (Gibson et al., 2021).



490  
491 Fig. 6. Appearance of bacteria (in this case, the marine microorganism *Collwellia psychrerythraea* 34H)  
492 under DHM with and without denoising. (a) Raw hologram of part of the microscopic field of view. (b)  
493 Median subtracted hologram (as in (Bedrossian, Wallace, Serabyn, Lindensmith and Nadeau, 2020)) showing  
494 individual cells whose Airy patterns overlap in Z. (c) Reconstruction on a single focal plane in amplitude.  
495 Cells in focus (arrow) are reduced to 1-2 pixels, while cells not in focus in that plane retain large diffraction  
496 patterns. (d) Phase reconstruction on a single Z plane, with an example cell indicated by an arrow, using a

497 reference hologram that is the mean of the entire stack. (e) YZ image through a stack of phase images  
498 reconstructed every 1  $\mu\text{m}$ , showing the Gouy phase anomaly. (f) Derivative image of cell in the YZ plane.  
499 (g) Derivative image of the same plane in XY with arrow indicating the same cell as in Panel (d).

500  
501 For 3D datasets of all types, *deconvolution* may be necessary to improve axial resolution, which  
502 is lower than lateral resolution for all microscopic techniques. Deconvolution is based upon  
503 knowing the shape of the point-spread function (PSF) for the microscope system, and reducing  
504 each PSF in the image to a point based upon this input. Exact algorithms depend upon the particular  
505 parameters of the PSF and the noise, and so are specific to each microscopy technique.  
506 Comprehensive, practical reviews are available for brightfield microscopy and fluorescence  
507 microscopy (Goodwin, 2014, Swedlow, 2013), as well as for more specialized techniques such as  
508 light sheet microscopy (Becker et al., 2019). The PSF may be experimentally measured by imaging  
509 unresolved point particles, or may be theoretically calculated based upon the optics of the  
510 microscope. Theoretical modeling of the PSF is done within the software with the user supplying  
511 values such as the objective lens, immersion medium, and illumination wavelength. Commercial  
512 packages and open-source plug-ins are available for deconvolution of fluorescence and brightfield  
513 images (Table III).

514 

#### 4.2. Cell detection

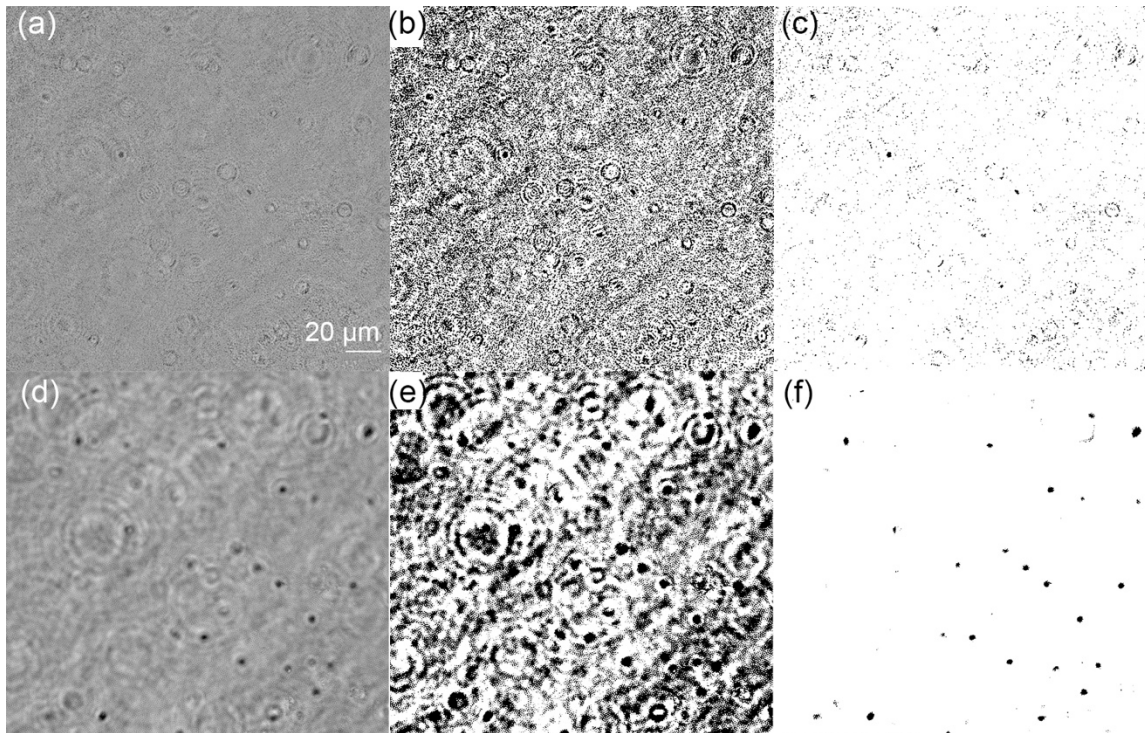
515 Cell detection consists of recognizing pixel clusters of a defined size, which stand out from the  
516 background in a way that may be identified by an algorithm. Frequently, but not always, images  
517 are thresholded and converted to binary before tracking. Thresholding of fluorescence images is  
518 fairly straightforward, but for low signal-to-noise techniques such as brightfield and DHM, cell  
519 detection may be the most challenging aspect of the data analysis. A recent review provided a  
520 detailed overview of techniques and software for microbial image analysis, including both single  
521 cell and community analysis (Jeckel and Drescher, 2021). For most tracking purposes, cells must

522 be accurately identified frame by frame; thus, the detection step is independent of, but necessary  
523 to, the tracking step.

524 *4.2.1. Detection by thresholding*

525 Because of the presence of Airy rings, phase contrast and DHM images cannot be thresholded  
526 readily (Fig. 7 (a)-(c)). The edges of the Airy rings are detected more easily by particle detection  
527 algorithms than the in-focus cells. Reconstructions of median-subtracted holograms, phase  
528 derivatives, or projections across multiple Z planes all permit thresholding for some datasets (with  
529 no general rule applicable to all). Projections across Z planes may be sums of all slices, maximum  
530 projections, or minimum projections, again depending upon the dataset. Thresholding based upon  
531 maximum entropy yields the best results for most brightfield images (**Figure 7 (d)-(f)**).

532



533  
534 Fig. 7. Thresholding DHM images of the bacterium *Shewanella putrefaciens*. (a) Amplitude reconstruction on a  
535 single focal plane. (b) Thresholding using the “default” algorithm in Fiji. (c) Thresholding using the “Max Entropy”  
536 algorithm in Fiji. (d) Sum of multiple Z planes from the same field of view. (e) Thresholding using the “default”  
537 algorithm. (f) Thresholding using Max Entropy identifies the majority of the cells and can be used for tracking.  
538

553 Convolutional neural networks (CNNs) are a type of machine learning algorithm that learns  
554 directly from image data. MATLAB includes a Deep Learning Toolbox that can be used to design,  
555 train, and apply CNNs. New software packages have also recently been reported for submicron  
556 particle tracking which have been shown to recognize non-spherical cells such as *Salmonella*  
557 (Newby et al., 2018).

558 4.3. Cell tracking

After particle identification, tracking still poses a challenge. While excellent tools exist for analyzing passive motion, such as Brownian motion, simple techniques such as nearest neighbor linking over the smallest Euclidean distance cannot be used for particle tracking with partly fast-moving, strongly accelerating microbes. Particle tracks intersect and overlap, and velocity vectors

are unpredictable. Therefore, the linking step is often done using a cost (or energy) function that takes into account velocity aspects (such as smoothness of the trajectory segment, smoothness of 3D velocity, smoothness, and upper bound conditions on accelerations) or morphological characteristics (cell size, shape, aspect). That means it requires *a priori* information about the microbes. However, the correct weighting of all the different features of the cost function is often highly dependent on the used set-up and requires a lot of fine-tuning.

569

### 4.3.1. *Manual tracking*

571 Manual tracking was the only possible approach before the development of high-performance  
572 computers (Berg and Brown, 1972, Schneider and Doetsch, 1974). Even with modern  
573 computation, it is still in widespread use, either as a stand-alone technique or to “ground truth”  
574 automated methods. Computational tools can assist with manual tracking by annotating and saving  
575 tracks. The technique is tedious and is frequently outsourced to data analysts or assigned to  
576 undergraduate students. Throughput is low.

577

### 4.3.2. Automated tracking

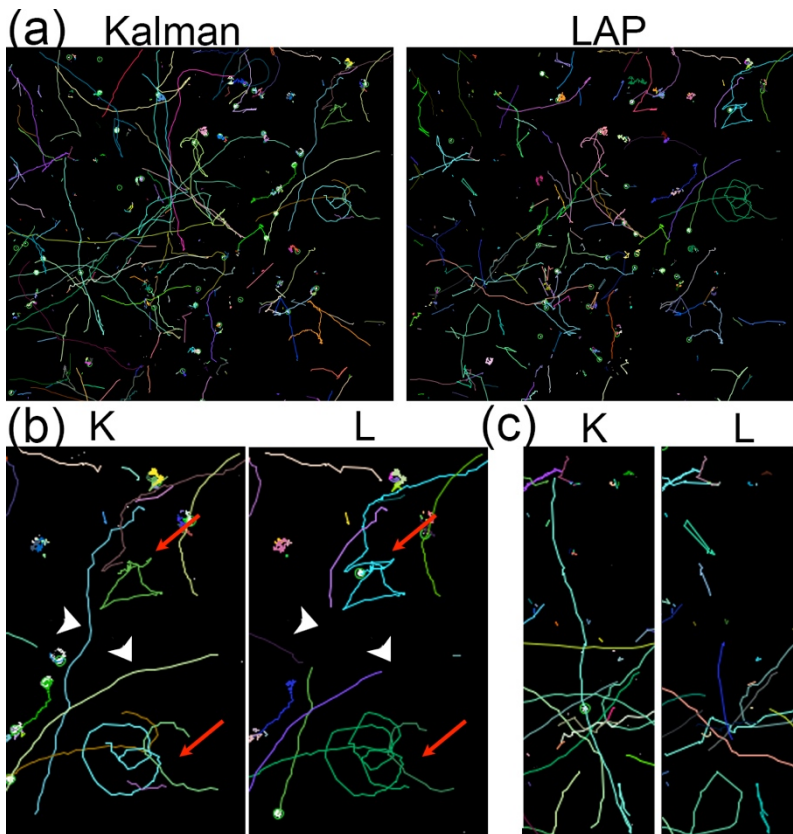
579 Automated tracking greatly decreases the workload and improves statistics. Common  
580 algorithms are discussed below.

581 The Linear Assignment Problem (LAP) tracker, published in 2008, helps solve the problems  
582 of trajectory overlap, particle disappearance from frame to frame, and trajectory merging and  
583 splitting(Jaqaman et al., 2008). Identified particles are linked frame to frame, then segments are  
584 linked to create trajectories. In order to determine whether segments belong to the same trajectory,  
585 a “cost matrix” is used representing all of the possibilities for spots in one frame to be linked to  
586 spots in the next. The matrix is minimized to create the most probable set of trajectories. In most  
587 software implementations, the user can fine-tune the algorithm by specifying the maximum

588 number of frames across which to link, and the maximum number of pixels traveled by a  
589 microorganism between frames. These parameters are obviously highly dependent upon the speed  
590 of the microorganism relative to the camera frame rate. For a heterogeneous mix of  
591 microorganisms of different speeds, the tracker may need to be re-run with different parameters to  
592 optimize linking for each cell type. The ability of the detection algorithm to find the cell in each  
593 frame will also influence the gap-closing parameter.

594 A second approach relies on a Kalman filter, reported in the same paper as the LAP tracker  
595 (Jaqaman, Loerke, Mettlen, Kuwata, Grinstein, Schmid and Danuser, 2008), to predict the most  
596 probable position of a particle assuming that it moves with a constant velocity. The same cost  
597 matrix is used as for LAP tracking, using the square distance as cost; the software should allow  
598 manual input of test values for this initial distance. The predicted positions are linked against the  
599 actual positions of particles in each successive frame.

600 Even for a homogeneous culture of a single bacterial species, there are some trajectories that  
601 are better captured with a LAP tracker (e.g., those with turns or spirals), and those better captured  
602 with the Kalman tracker (long runs) (Fig. 8). In all cases, several iterations will likely be necessary  
603 to optimize gap-closing distances, and manual editing and stitching/cutting of tracks can further  
604 improve results after the automated detection.



605  
606 Fig. 8. Kalman vs. LAP tracker for DHM data using the microorganism *Shewanella putrefaciens*. (a) Large field of  
607 view indicating how it is possible to tell at a glance that the Kalman filter detects more long runs than the LAP  
608 tracker. (b) 2-fold zoom of upper right of image, showing circuitous tracks that were captured as single tracks by the  
609 LAP tracker but not the Kalman filter (red arrows), vs. long runs that were successfully captured by the Kalman  
610 filter but broken in the LAP tracker (white arrowheads). (c) 2-fold zoom of lower left corner showing a long track  
611 apparent in the Kalman filter (turquoise) that was entirely missed by the LAP tracker. The accuracy of the  
612 assignments must be checked by eye (see Supplementary Videos 1 and 2 for animations of Panel (a)).  
613

614 Software packages of particular relevance to all steps of data processing, bacterial identification

615 and tracking are tabulated in Table III.

#### 616 4.4. Considerations for 3D

617 3D tracking of microbial motility can lead to more accurate velocity measurements as well as

618 reveal features that are obscured by 2D projections, especially dynamic surface behavior (Bianchi

619 et al., 2019) (Taute, Gude, Tans and Shimizu, 2015). However, 3D tracking poses particular

620 difficulties, and so full 3D tracked datasets of micron-sized organisms are sparse. The two biggest

621 issues with 3D tracking are (1) poorer axial resolution vs XY resolution with most microscopic

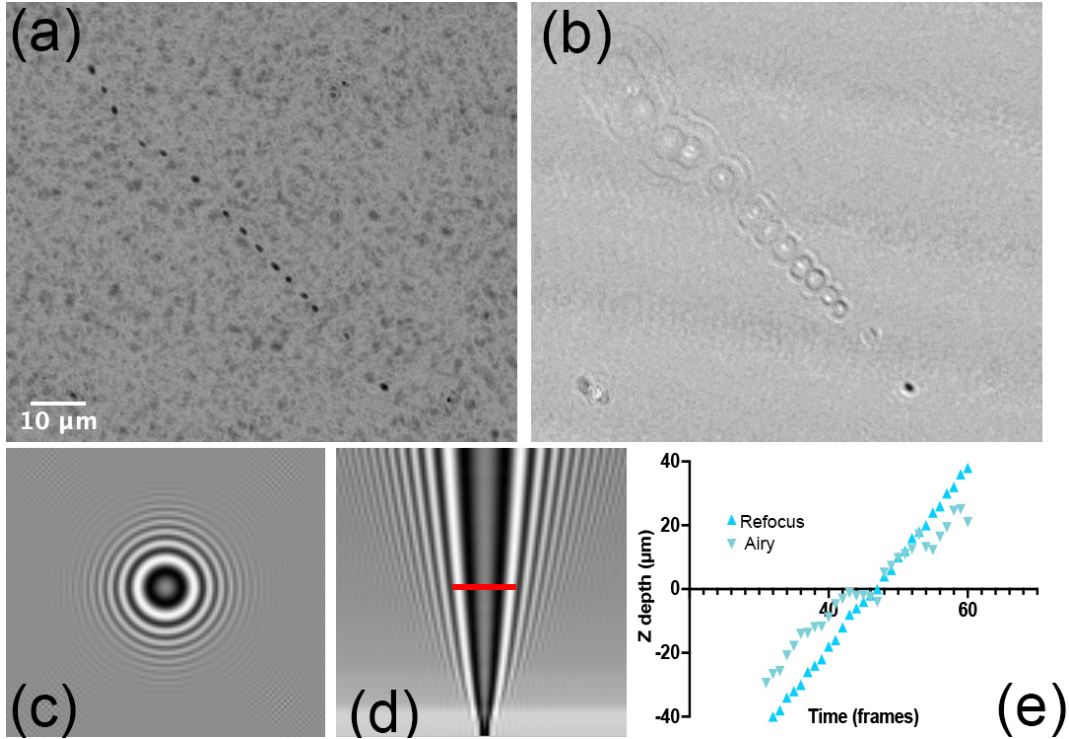
622 techniques; and (2) large dataset size. The use of supercomputers and software/file types

623 specifically designed for handling large datasets can permit tracking of full resolution  
624 (2048x2048x100 XYZ) data, but usually either downsampling, cropping, or truncation of time  
625 series is necessary. Truncation or cropping may be designed to isolate a specific cell. Stitching  
626 may be done in spatial or time coordinates depending upon which is easier for the given data.

627 Alternatives to tracking of full 3D datasets include:

- 628 • 2D tracking of Z-projections followed by manual extraction of Z coordinates (Fig. 9 (a),  
629 Supplementary Video 3) (Acres and Nadeau, 2021).
- 630 • 2D tracking of Z-projections followed by automated extraction of Z coordinates by  
631 fitting or measuring Airy rings; may be done for phase contrast and DHM (Fig. 9 (b),  
632 Supplementary Video 4). For DHM, a simulated PSF may be created by angular  
633 spectrum propagation of a single-pixel spot (Piedrahita-Quintero et al., 2015) (Fig. 9  
634 (c), (d)), and then used to match experimental data (Fig. 9 (e)).
- 635 • Tracking of XY and XZ or YZ projections, then matching corresponding coordinates to  
636 obtain full XYZ information. However, the overlapping coordinates to obtain full tracks  
637 can be challenging; this approach is much more efficient with passive motion, where  
638 corresponding X or Y coordinates can be readily mapped (Rouzie and Lindensmith,  
639 2021).

640 Note that none of these approaches are high throughput. All require substantial cropping of the  
641 datasets to make them manageable in size, as well as user input to ensure that the correct cell is  
642 tracked throughout the length of its appearance in the volume of view.



643 Fig. 9. Obtaining Z coordinates from DHM reconstructions. (a) Minimum intensity projection of 30 frames of a  
 644 single cell, choosing the z plane at which the cell is in best focus (all slices shown in Supplementary Video 3). (b)  
 645 Minimum plus maximum intensity projection for the same cell from a reconstruction at a single focal plane (all  
 646 slices shown in Supplementary Video 4). (c) Simulated Airy rings in the XY plane for a point source projected over  
 647 30  $\mu\text{m}$  in Z, using angular spectrum propagation with the same optical parameters as the instrument used to collect  
 648 the experimental data. (d) Simulated Airy rings in the YZ plane; the red line indicates the area that was used to  
 649 estimate depth for the cell at each time point. (e) Depth obtained with time for the tracked cell, comparing the  
 650 refocusing and Airy ring approaches.

652 **4.5. Analyzing tracks**

653 Unlike simple physical motion such as Brownian motion, active motility displays both physical  
 654 and physiological features that have not been fully elucidated. To mention a few examples, the  
 655 run-reverse-flick swimming pattern of bacteria with a single polar flagellum was not described  
 656 until 2011 (Stocker, 2011). Persistence in tracks was first reported in 2013 (Rosser et al., 2013).  
 657 Tumbling frequencies near a surface, suggesting chemotactic behavior, were reported in 2020  
 658 (Lemelle et al., 2020). The biophysics underlying bacterial motility can be lost if tracks are  
 659 fragmented, spurious, or if they miss key features such as reorientation events. There is no  
 660 established standard for quantifying bacterial reorientations. Because of the different possible

661 motility patterns as shown in Fig. 1, such analysis must be strain-dependent. This becomes  
662 increasingly challenging if the culture represents a mix of species. All tracking methods lead to  
663 some degree of false negative and false positive detection, and all require manual editing to stitch  
664 fragmented tracks or separate spuriously joined tracks. In some cases, this will require almost as  
665 much work as full manual tracking.

666 Parameters that may need to be quantified include run lengths, tumbles and/or reversals, turn  
667 angles, velocity, acceleration, and correlation coefficients. All of these parameters, if they are  
668 reported as averages over individual tracks, can be highly misleading if the tracks are spuriously  
669 truncated, joined, or split. Another aspect that must be considered is that bacterial cultures contain  
670 some fraction of non-motile cells, and the extent to which these should be analyzed or excluded  
671 from analysis depends upon the experiments and the hypotheses being tested. The degree to which  
672 false negatives/positives and broken tracks can be tolerated also depends upon what is being  
673 studied.

674 When tracks are correctly identified and exported as XYT or XYZT coordinates, parameters  
675 such as velocities and accelerations may be readily calculated from their definitions. However,  
676 evaluation of complex behaviors such as chemotaxis (Pohl et al., 2017) and tumbling (Liang et al.,  
677 2018) require models and model-based parameters, and their analysis can be assisted by  
678 specialized software packages as indicated in Table III.

679

Software	Task	Platform	Availability
TrackMate <sup>a</sup>	Particle identification and tracking	Fiji	Open source
Arivis Vision 4D <sup>b</sup>	Many filters and tracking algorithms; handles large 4D stacks	Win	Commercial
MOSAICSuite <sup>c</sup>	Particle detection and tracking	Fiji	Open source
Ilastik <sup>d</sup>	Machine learning for segmentation	Fiji	Open source
MorphoLibJ <sup>e</sup>	Morphology analysis	Fiji	Open source
SuperSegger <sup>f</sup>	Cell segmentation (fluorescence)	MATLAB	Free
MicrobeJ <sup>g</sup>	Cell detection and analysis; large datasets	Fiji	Open source
DeepBacs <sup>h</sup>	Deep learning segmentation for fluorescence & brightfield	Jupyter	
Zcells <sup>i</sup>	Machine-learning based segmentation	MATLAB	Free
TumbleScore <sup>j</sup>	Bacterial tracking and track analysis	MATLAB	Free
Your Software for Motility Recognition <sup>k</sup>	High-throughput bacterial identification and tracking	Python	Open source
Bacterial swarming <sup>l</sup>	Swarming segmentation and analysis	MATLAB	Free
AI Tracking solutions <sup>m</sup>	CNN-based tracking	Cloud-based	Commercial
Machine Learning Object Tracking (MLOT) <sup>n</sup>	Machine learning based identification	MATLAB	Free
TaxisPy <sup>o</sup>	Chemotaxis analysis	Python	Free
DHM <sup>p</sup>	DHM reconstruction/simulation	Fiji	Open source
DHM Utilities <sup>q</sup>	DHM reconstruction with reference hologram options	Fiji	Open source
KOALA <sup>r</sup>	DHM reconstruction with reference hologram options	Win	Commercial
Iterative Deconvolve 3D <sup>s</sup>	Deconvolution	Fiji	Open source
DeconvolutionLab2 <sup>t</sup>	Deconvolution	Fiji	Open source
Huygens <sup>u</sup>	Deconvolution	Cross-platform (Win, Mac, Linux)	Commercial

Table III. Selected software packages for image processing, bacterial detection, and tracking.

<sup>a</sup> D. Ershov *et al.*, *Nat Methods* **19**, 829 (2022)

<sup>b</sup> <https://www.arivis.com/solutions/vision4d>

<sup>c</sup> I. F. Sbalzarini and P. Koumoutsakos, *Journal of Structural Biology* **151**, 182 (2005)

<sup>d</sup> S. Berg *et al.*, *Nat Methods* **16**, 1226 (2019)

<sup>e</sup> D. Legland *et al.*, *Bioinformatics* **32**, 3532 (2016)

<sup>f</sup> S. Stylianidou *et al.*, *Mol Microbiol* **102**, 690 (2016)

<sup>g</sup> A. Ducret *et al.*, *Nat Microbiol* **1**, 16077 (2016)

<sup>h</sup> C. Spahn *et al.*, *Commun Biol* **5**, 688 (2022)

<sup>i</sup> <https://lab513.github.io/Zcells/>

<sup>j</sup> A. E. Pottash *et al.*, *Biotechniques* **62**, 31 (2017)

<sup>k</sup> J. Schwanbeck *et al.*, *BMC Bioinformatics* **21**, 166 (2020)

<sup>l</sup> A. Be'er *et al.*, *Communications Physics* **3**, 66 (2020)

<sup>m</sup> <https://aitracker.net/>

<sup>n</sup> <https://github.com/mbedross/MachineLearningObjectTracking>

<sup>o</sup> M. A. Valderrama-Gomez *et al.*, *J Microbiol Methods* **175**, 105918 (2020)

<sup>p</sup> <https://github.com/unal-optodigital/DHM/blob/master/README.md>

697 <sup>q</sup> <https://github.com/sudgy>  
698 <sup>r</sup> <https://www.lynceetec.com/koala-acquisition-analysis/>  
699 <sup>s</sup> <https://imagej.net/plugins/iterative-deconvolve-3d>  
700 <sup>t</sup> Sage *et al. Methods* **115**, 28-41, doi:10.1016/j.ymeth.2016.12.015 (2017)  
701 <sup>u</sup> <https://svi.nl/Huygens-Software>  
702  
703

704 **5. Conclusion**

705 Tracking bacteria still represents a challenge, especially in 3D or under extreme conditions such  
706 as high or low temperature, high cell speed, or dense or inhomogeneous cultures (mixed species  
707 or phenotypes). Each experimental type, or even each dataset, will require customized methods  
708 and ground-truthing to eliminate false negatives and false positives. Manual tracking remains a  
709 necessary task for many applications, since the human eye and brain can identify cells and motion  
710 in noisy environments where even the most sophisticated algorithms fail. Modeling the physics of  
711 motility can be influenced by false positives, false negatives, and broken tracks. Improvements in  
712 3D tracking will lead to new discoveries in the physics of microbial motility.

713  
714  
715 **ACKNOWLEDGEMENTS**

716 The authors acknowledge the support of the National Science Foundation (Grant No. 1828793).  
717 Portions of this work were supported under a contract from the Jet Propulsion Laboratory,  
718 California Institute of Technology, under a contract with the National Aeronautics and Space  
719 Administration.

720  
721  
722  
723

724 **References**  
725

726 Acres, J., Nadeau, J., 2021. 2D vs 3D Tracking in Bacterial Motility Analysis. *AIMS Biophysics*.  
727 8, 385-399.

728 Albers, C.N., Kramshøj, M., Rinnan, R., 2018. Rapid mineralization of biogenic volatile organic  
729 compounds in temperate and Arctic soils. *Biogeosciences*. 15, 3591-3601.

730 Albers, S.V., Jarrell, K.F., 2015. The archaellum: how Archaea swim. *Front Microbiol*. 6, 23.

731 Armitage, J.P., 1999. Bacterial Tactic Responses. In: R. K. Poole (Ed.), *Advances in Microbial  
732 Physiology*, Vol. 41, Academic Press, pp. 229-289.

733 Armitage, J.P., Schmitt, R., 1997. Bacterial chemotaxis: *Rhodobacter sphaeroide* and  
734 *Sinorhizobium meliloti* - variations on a theme? *Microbiology*. 143, 3671-3682.

735 Bardy, S.L., Briegel, A., Rainville, S., Krell, T., 2017. Recent Advances and Future Prospects in  
736 Bacterial and Archaeal Locomotion and Signal Transduction. *Journal of Bacteriology*. 199,  
737 JB.00203-00217.

738 Becker, K., Saghafi, S., Pende, M., Sabdyusheva-Litschauer, I., Hahn, C.M., Foroughipour, M.,  
739 Jahrling, N., Dodt, H.U., 2019. Deconvolution of light sheet microscopy recordings. *Sci Rep*. 9,  
740 17625.

741 Bedrossian, M., Wallace, J.K., Serabyn, E., Lindensmith, C., Nadeau, J., 2020. Enhancing final  
742 image contrast in off-axis digital holography using residual fringes. *Opt Express*. 28, 16764-  
743 16771.

744 Bente, K., Mohammadinejad, S., Charsooghi, M.A., Bachmann, F., Codutti, A., Lefevre, C.T.,  
745 Klumpp, S., Faivre, D., 2020. High-speed motility originates from cooperatively pushing and  
746 pulling flagella bundles in bilophotrichous bacteria. *Elife*. 9.

747 Berg, H.C., 1971. How to Track Bacteria. *Review of Scientific Instruments*. 42, 868-871.

748 Berg, H.C., Brown, D.A., 1972. Chemotaxis in *Escherichia coli* analysed by three-dimensional  
749 tracking. *Nature*. 239, 500-504.

750 Berg, H.C., Brown, D.A., 1974. Chemotaxis in *Escherichia coli* analyzed by three-dimensional  
751 tracking. *Antibiot Chemother* (1971). 19, 55-78.

752 Bernas, T., Zarebski, M., Dobrucki, J.W., Cook, P.R., 2004. Minimizing photobleaching during  
753 confocal microscopy of fluorescent probes bound to chromatin: role of anoxia and photon flux. *J  
754 Microsc.* 215, 281-296.

755 Bianchi, S., Saglimbeni, F., Frangipane, G., Dell'Arciprete, D., Di Leonardo, R., 2019. 3D  
756 dynamics of bacteria wall entrapment at a water-air interface. *Soft Matter*. 15, 3397-3406.

757 Boquet-Pujadas, A., Olivo-Marin, J.C., Guillen, N., 2021. Bioimage Analysis and Cell Motility.  
758 Patterns (N Y). 2, 100170.

759 Boudreau, C., Wee, T.L., Duh, Y.R., Couto, M.P., Ardakani, K.H., Brown, C.M., 2016.  
760 Excitation Light Dose Engineering to Reduce Photo-bleaching and Photo-toxicity. *Sci Rep*. 6,  
761 30892.

762 Buitrago-Duque, C., Garcia-Sucerquia, J., 2022. Realistic simulation and real-time  
763 reconstruction of digital holographic microscopy experiments in ImageJ. *Appl. Opt.* 61, B56-  
764 B63.

765 Charles-Orszag, A., Lord, S.J., Mullins, R.D., 2021. High-Temperature Live-Cell Imaging of  
766 Cytokinesis, Cell Motility, and Cell-Cell Interactions in the Thermoacidophilic Crenarchaeon  
767 *Sulfolobus acidocaldarius*. *Front Microbiol*. 12, 707124.

768 Chenouard, N., Smal, I., de Chaumont, F., Maska, M., Sbalzarini, I.F., Gong, Y., Cardinale, J.,

769 Carthel, C., Coraluppi, S., Winter, M., Cohen, A.R., Godinez, W.J., Rohr, K., Kalaidzidis, Y.,

770 Liang, L., Duncan, J., Shen, H., Xu, Y., Magnusson, K.E., Jalden, J., Blau, H.M., Paul-

771 Gilloteaux, P., Roudot, P., Kervrann, C., Waharte, F., Tinevez, J.Y., Shorte, S.L., Willemse, J.,

772 Celler, K., van Wezel, G.P., Dan, H.W., Tsai, Y.S., Ortiz de Solorzano, C., Olivo-Marin, J.C.,

773 Meijering, E., 2014. Objective comparison of particle tracking methods. *Nat Methods.* 11, 281-

774 289.

775 Cheong, F.C., Sun, B., Dreyfus, R., Amato-Grill, J., Xiao, K., Dixon, L., Grier, D.G., 2009. Flow

776 visualization and flow cytometry with holographic video microscopy. *Opt Express.* 17, 13071-

777 13079.

778 Chia, H.E., Marsh, E.N.G., Biteen, J.S., 2019. Extending fluorescence microscopy into anaerobic

779 environments. *Curr Opin Chem Biol.* 51, 98-104.

780 Chia, H.E., Zuo, T., Koropatkin, N.M., Marsh, E.N.G., Biteen, J.S., 2020. Imaging living

781 obligate anaerobic bacteria with bilin-binding fluorescent proteins. *Curr Res Microb Sci.* 1, 1-6.

782 Cohoe, D., Hanczarek, I., Wallace, J.K., Nadeau, J., 2019. Multiwavelength Digital Holographic

783 Imaging and Phase Unwrapping of Protozoa Using Custom Fiji Plug-ins. *Frontiers in Physics.* 7.

784 Colomb, T., Kuhn, J., Charriere, F., Depeursinge, C., Marquet, P., Aspert, N., 2006. Total

785 aberrations compensation in digital holographic microscopy with a reference conjugated

786 hologram. *Opt Express.* 14, 4300-4306.

787 Corkidi, G., Taboada, B., Wood, C.D., Guerrero, A., Darszon, A., 2008. Tracking sperm in

788 three-dimensions. *Biochem Biophys Res Commun.* 373, 125-129.

789 Davidson, M.W., Spring, K.R., Nikon Microscopy U.

790 de Chaumont, F., Dallongeville, S., Chenouard, N., Herve, N., Pop, S., Provoost, T., Meas-  
791 Yedid, V., Pankajakshan, P., Lecomte, T., Le Montagner, Y., Lagache, T., Dufour, A., Olivo-  
792 Marin, J.C., 2012. Icy: an open bioimage informatics platform for extended reproducible  
793 research. *Nat Methods.* 9, 690-696.

794 Deter, H.S., Dies, M., Cameron, C.C., Butzin, N.C., Buceta, J., 2019. A Cell  
795 Segmentation/Tracking Tool Based on Machine Learning. *Methods Mol Biol.* 2040, 399-422.

796 Dubay, M.M., Johnston, N., Wronkiewicz, M., Lee, J., Lindensmith, C.A., Nadeau, J.L., 2022.  
797 Quantification of Motility in *Bacillus subtilis* at Temperatures Up to 84°C Using a Submersible  
798 Volumetric Microscope and Automated Tracking *Frontiers in Microbiology.* 13.

799 Edelstein, A., Amodaj, N., Hoover, K., Vale, R., Stuurman, N., 2010. Computer control of  
800 microscopes using microManager. *Curr Protoc Mol Biol.* Chapter 14, Unit14 20.

801 El Najjar, N., van Teeseling, M.C.F., Mayer, B., Hermann, S., Thanbichler, M., Graumann, P.L.,  
802 2020. Bacterial cell growth is arrested by violet and blue, but not yellow light excitation during  
803 fluorescence microscopy. *BMC Mol Cell Biol.* 21, 35.

804 Emami, N., Sedaei, Z., Ferdousi, R., 2021. Computerized cell tracking: Current methods, tools  
805 and challenges. *Visual Informatics.* 5, 1-13.

806 Farhadi, A., Bedrossian, M., Lee, J., Ho, G.H., Shapiro, M.G., Nadeau, J.L., 2020. Genetically  
807 Encoded Phase Contrast Agents for Digital Holographic Microscopy. *Nano Letters.* 20, 8127-  
808 8134.

809 Fregoso, S.F., Lima, F., Wallace, J.K., Bedrossian, M., McKeithen, D., Kettenbeil, C., Loya, F.,  
810 Lindensmith, C., 2020. DHMx (Digital Holographic Microscope Experience) Software Tool,  
811 Imaging and Applied Optics Congress, Optica Publishing Group, Washington, DC, pp. HF2G.7.

812 Frymier, P.D., Ford, R.M., Berg, H.C., Cummings, P.T., 1995. Three-dimensional tracking of  
813 motile bacteria near a solid planar surface. *Proc Natl Acad Sci U S A.* 92, 6195-6199.

814 Gahlmann, A., Moerner, W.E., 2014. Exploring bacterial cell biology with single-molecule  
815 tracking and super-resolution imaging. *Nat Rev Microbiol.* 12, 9-22.

816 Galande, A.S., Thapa, V., Ram, H.P., John, R., 2021. Untrained Neural Network with Explicit  
817 Denoiser For Lensless Inline Holographic Microscopy. In: H. J. B. M.-C. M. M. O. S. A. T. S. A.  
818 T. K. J. W. F. O. F. S. P. B. P. Hua, O. Korotkova (Eds.), *OSA Imaging and Applied Optics*  
819 Congress 2021 (3D, COSI, DH, ISA, pcAOP), Optica Publishing Group, Washington, DC, pp.  
820 CTh7A.7.

821 Gibson, T., Bedrossian, M., Serabyn, E., Lindensmith, C., Nadeau, J.L., 2021. Using the Gouy  
822 phase anomaly to localize and track bacteria in digital holographic microscopy 4D images. *J Opt*  
823 *Soc Am A Opt Image Sci Vis.* 38, A11-A18.

824 Giloh, H., Sedat, J.W., 1982. Fluorescence microscopy: reduced photobleaching of rhodamine  
825 and fluorescein protein conjugates by n-propyl gallate. *Science.* 217, 1252-1255.

826 Goodwin, P.C., 2014. Quantitative deconvolution microscopy. *Methods Cell Biol.* 123, 177-192.

827 Harrison, J.U., Baker, R.E., 2018. The impact of temporal sampling resolution on parameter  
828 inference for biological transport models. *PLoS Comput Biol.* 14, e1006235.

829 Herzog, B., Wirth, R., 2012. Swimming Behavior of Selected Species of Archaea. *Applied and*  
830 *Environmental Microbiology.* 78, 1670-1674.

831 Herzog, B., Wirth, R., 2012. Swimming behavior of selected species of Archaea. *Appl Environ*  
832 *Microbiol.* 78, 1670-1674.

833 Holscher, H.D., 2017. Dietary fiber and prebiotics and the gastrointestinal microbiota. Gut  
834 Microbes. 8, 172-184.

835 Jaqaman, K., Loerke, D., Mettlen, M., Kuwata, H., Grinstein, S., Schmid, S.L., Danuser, G.,  
836 2008. Robust single-particle tracking in live-cell time-lapse sequences. Nature Methods. 5, 695-  
837 702.

838 Jeckel, H., Drescher, K., 2021. Advances and opportunities in image analysis of bacterial cells  
839 and communities. FEMS Microbiol Rev. 45.

840 Junge, K., Eicken, H., Deming, J.W., 2003. Motility of *Colwellia psychrerythraea* strain 34H at  
841 subzero temperatures. Appl Environ Microbiol. 69, 4282-4284.

842 Ko, S., Jeon, H., Yoon, S., Kyung, M., Yun, H., Na, J.H., Jung, S.T., 2020. Discovery of Novel  
843 *Pseudomonas putida* Flavin-Binding Fluorescent Protein Variants with Significantly Improved  
844 Quantum Yield. J Agric Food Chem. 68, 5873-5879.

845 Kühn, J., Niraula, B., Liewer, K., Kent Wallace, J., Serabyn, E., Graff, E., Lindensmith, C.,  
846 Nadeau, J.L., 2014. A Mach-Zender digital holographic microscope with sub-micrometer  
847 resolution for imaging and tracking of marine micro-organisms. Review of Scientific  
848 Instruments. 85, 123113.

849 Kuhn, M.J., Schmidt, F.K., Farthing, N.E., Rossmann, F.M., Helm, B., Wilson, L.G., Eckhardt,  
850 B., Thormann, K.M., 2018. Spatial arrangement of several flagellins within bacterial flagella  
851 improves motility in different environments. Nat Commun. 9, 5369.

852 Latychevskaia, T., Fink, H.-W., 2009. Simultaneous reconstruction of phase and amplitude  
853 contrast from a single holographic record. Optics Express. 17, 10697-10705.

854 Lee, S.-H., Roichman, Y., Yi, G.-R., Kim, S.-H., Yang, S.-M., Blaaderen, A.v., Oostrum, P.v.,

855 Grier, D.G., 2007. Characterizing and tracking single colloidal particles with video holographic

856 microscopy. *Optics Express*. 15, 18275-18282.

857 Lee, S.H., Roichman, Y., Yi, G.R., Kim, S.H., Yang, S.M., van Blaaderen, A., van Oostrum, P.,

858 Grier, D.G., 2007. Characterizing and tracking single colloidal particles with video holographic

859 microscopy. *Opt Express*. 15, 18275-18282.

860 Lei, H., Hu, X., Zhu, P., Chang, X., Zeng, Y., Hu, C., Li, H., Hu, X., 2015. Nano-level position

861 resolution for particle tracking in digital in-line holographic microscopy. *Journal of Microscopy*.

862 260, 100-106.

863 Lemelle, L., Cajgfinger, T., Nguyen, C.C., Dominjon, A., Place, C., Chatre, E., Barbier, R.,

864 Palierne, J.F., Vaillant, C., 2020. Tumble Kinematics of Escherichia coli near a Solid Surface.

865 *Biophys J.* 118, 2400-2410.

866 Leuko, S., Legat, A., Fendrihan, S., Stan-Lotter, H., 2004. Evaluation of the LIVE/DEAD

867 BacLight kit for detection of extremophilic archaea and visualization of microorganisms in

868 environmental hypersaline samples. *Appl Environ Microbiol.* 70, 6884-6886.

869 Liang, X., Lu, N., Chang, L.C., Nguyen, T.H., Massoudieh, A., 2018. Evaluation of bacterial run

870 and tumble motility parameters through trajectory analysis. *J Contam Hydrol.* 211, 26-38.

871 Lindensmith, C.A., Rider, S., Bedrossian, M., Wallace, J.K., Serabyn, E., Showalter, G.M.,

872 Deming, J.W., Nadeau, J.L., 2016. A Submersible, Off-Axis Holographic Microscope for

873 Detection of Microbial Motility and Morphology in Aqueous and Icy Environments. *PLoS One*.

874 11, e0147700.

875 Liu, B., Gulino, M., Morse, M., Tang, J.X., Powers, T.R., Breuer, K.S., 2014. Helical motion of  
876 the cell body enhances *Caulobacter crescentus* motility. *Proc Natl Acad Sci U S A.* 111, 11252-  
877 11256.

878 Manuel, B., Marwan, E.-K., Daniel, N., Jay, N., 2018. A machine learning algorithm for  
879 identifying and tracking bacteria in three dimensions using Digital Holographic Microscopy.  
880 *AIMS Biophysics.* 5, 36-49.

881 Marquet, P., Rappaz, B., Magistretti, P.J., Cuche, E., Emery, Y., Colomb, T., Depeursinge, C.,  
882 2005. Digital holographic microscopy: a noninvasive contrast imaging technique allowing  
883 quantitative visualization of living cells with subwavelength axial accuracy. *Opt Lett.* 30, 468-  
884 470.

885 Martin, J.P., Logsdon, N., 1987. Oxygen radicals mediate cell inactivation by acridine dyes,  
886 fluorescein, and lucifer yellow CH. *Photochem Photobiol.* 46, 45-53.

887 Martinez, V.A., Besseling, R., Croze, O.A., Tailleur, J., Reufer, M., Schwarz-Linek, J., Wilson,  
888 L.G., Bees, M.A., Poon, W.C., 2012. Differential dynamic microscopy: a high-throughput  
889 method for characterizing the motility of microorganisms. *Biophys J.* 103, 1637-1647.

890 Maslov, I., Bogorodskiy, A., Mishin, A., Okhrimenko, I., Gushchin, I., Kalenov, S., Dencher,  
891 N.A., Fahlke, C., Buldt, G., Gordeliy, V., Gensch, T., Borshchevskiy, V., 2018. Efficient non-  
892 cytotoxic fluorescent staining of halophiles. *Sci Rep.* 8, 2549.

893 Meacock, O.J., Durham, W.M., 2021. Tracking bacteria at high density with FAST, the Feature-  
894 Assisted SegmenteTracker. *bioRxiv*, 2021.2011.2026.470050.

895 Micó, V., García, J., Camacho, L., Zalevsky, Z., 2011. Quantitative Phase Imaging in  
896 Microscopy Using a Spatial Light Modulator. In: P. Ferraro, A. Wax, Z. Zalevsky (Eds.),

897 Coherent Light Microscopy: Imaging and Quantitative Phase Analysis, Springer Berlin  
898 Heidelberg, Berlin, Heidelberg, pp. 145-167.

899 Miyata, M., Robinson, R.C., Uyeda, T.Q.P., Fukumori, Y., Fukushima, S.I., Haruta, S., Homma,  
900 M., Inaba, K., Ito, M., Kaito, C., Kato, K., Kenri, T., Kinosita, Y., Kojima, S., Minamino, T.,  
901 Mori, H., Nakamura, S., Nakane, D., Nakayama, K., Nishiyama, M., Shibata, S., Shimabukuro,  
902 K., Tamakoshi, M., Taoka, A., Tashiro, Y., Tulum, I., Wada, H., Wakabayashi, K.I., 2020. Tree  
903 of motility – A proposed history of motility systems in the tree of life. *Genes to Cells*. 25, 6-21.

904 Myung, K.K., 2010. Principles and techniques of digital holographic microscopy. *SPIE Reviews*.  
905 1, 018005.

906 Nadeau, J.L., Bin Cho, Y., Kuhn, J., Liewer, K., 2016. Improved Tracking and Resolution of  
907 Bacteria in Holographic Microscopy Using Dye and Fluorescent Protein Labeling. *Frontiers in*  
908 *Chemistry*. 4.

909 Najafi, J., Shaebani, M.R., John, T., Altegoer, F., Bange, G., Wagner, C., 2018. Flagellar number  
910 governs bacterial spreading and transport efficiency. *Science Advances*. 4, eaar6425.

911 Nan, B., Zusman, D.R., 2016. Novel mechanisms power bacterial gliding motility. *Molecular*  
912 *Microbiology*. 101, 186-193.

913 Newby, J.M., Schaefer, A.M., Lee, P.T., Forest, M.G., Lai, S.K., 2018. Convolutional neural  
914 networks automate detection for tracking of submicron-scale particles in 2D and 3D. *Proc Natl*  
915 *Acad Sci U S A*. 115, 9026-9031.

916 O'Connor, O.M., Alnahhas, R.N., Lugagne, J.B., Dunlop, M.J., 2022. DeLTA 2.0: A deep  
917 learning pipeline for quantifying single-cell spatial and temporal dynamics. *PLoS Comput Biol*.  
918 18, e1009797.

919 Pané, S., Puigmartí-Luis, J., Bergeles, C., Chen, X.-Z., Pellicer, E., Sort, J., Počepcová, V.,

920 Ferreira, A., Nelson, B.J., 2019. Imaging Technologies for Biomedical Micro- and

921 Nanoswimmers. *Advanced Materials Technologies*. 4, 1800575.

922 Peng, G., Caojin, Y., 2022. Resolution enhancement of digital holographic microscopy via

923 synthetic aperture: a review. *Light: Advanced Manufacturing*. 3, 105-120.

924 Piedrahita-Quintero, P., Castaneda, R., Garcia-Sucerquia, J., 2015. Numerical wave propagation

925 in ImageJ. *Appl Opt.* 54, 6410-6415.

926 Piepenbrink, K.H., Lillehoj, E., Harding, C.M., Labonte, J.W., Zuo, X., Rapp, C.A., Munson,

927 R.S., Goldblum, S.E., Feldman, M.F., Gray, J.J., Sundberg, E.J., 2016. Structural Diversity in the

928 Type IV Pili of Multidrug-resistant *Acinetobacter*. *Journal of Biological Chemistry*. 291, 22924-

929 22935.

930 Pohl, O., Hintsche, M., Alirezaeizanjani, Z., Seyrich, M., Beta, C., Stark, H., 2017. Inferring the

931 Chemotactic Strategy of *P. putida* and *E. coli* Using Modified Kramers-Moyal Coefficients.

932 *PLoS Comput Biol.* 13, e1005329.

933 Pollitt, E.J.G., Diggle, S.P., 2017. Defining motility in the Staphylococci. *Cellular and Molecular*

934 *Life Sciences*. 74, 2943-2958.

935 Rappaz, B., Marquet, P., Cuche, E., Emery, Y., Depeursinge, C., Magistretti, P., 2005.

936 Measurement of the integral refractive index and dynamic cell morphometry of living cells with

937 digital holographic microscopy. *Opt Express*. 13, 9361-9373.

938 Rastadter, K., Tramontano, A., Wurm, D.J., Spadiut, O., Quehenberger, J., 2022. Flow

939 cytometry-based viability staining: an at-line tool for bioprocess monitoring of *Sulfolobus*

940 *acidocaldarius*. *AMB Express*. 12, 107.

941 Rosser, G., Fletcher, A.G., Wilkinson, D.A., de Beyer, J.A., Yates, C.A., Armitage, J.P., Maini,  
942 P.K., Baker, R.E., 2013. Novel methods for analysing bacterial tracks reveal persistence in  
943 *Rhodobacter sphaeroides*. PLoS Comput Biol. 9, e1003276.

944 Rouzie, D., Lindensmith, C.N., Jay, 2021. Microscopic Object Classification through Passive  
945 Motion Observations with Holographic Microscopy, Life, Vol. 11.

946 Ruffner, D.B., Cheong, F.C., Blusewicz, J.M., Philips, L.A., 2018. Lifting degeneracy in  
947 holographic characterization of colloidal particles using multi-color imaging. Optics express. 26,  
948 13239-13251.

949 Schindelin, J., Arganda-Carreras, I., Frise, E., Kaynig, V., Longair, M., Pietzsch, T., Preibisch,  
950 S., Rueden, C., Saalfeld, S., Schmid, B., Tinevez, J.Y., White, D.J., Hartenstein, V., Eliceiri, K.,  
951 Tomancak, P., Cardona, A., 2012. Fiji: an open-source platform for biological-image analysis.  
952 Nature methods. 9, 676-682.

953 Schnars, U., Jüptner, W.P., 2002. Digital recording and numerical reconstruction of holograms.  
954 Measurement science and technology. 13, R85.

955 Schneider, W.R., Doetsch, R.N., 1974. Velocity measurements of motile bacteria by use of a  
956 videotape recording technique. Appl Microbiol. 27, 283-284.

957 Schuech, R., Hoehfertner, T., Smith, D.J., Humphries, S., 2019. Motile curved bacteria are  
958 Pareto-optimal. Proceedings of the National Academy of Sciences. 116, 14440-14447.

959 Sirico, D.G., Miccio, L., Wang, Z., Memmolo, P., Xiao, W., Che, L., Xin, L., Pan, F., Ferraro,  
960 P., 2022. Compensation of aberrations in holographic microscopes: main strategies and  
961 applications. Applied Physics B. 128, 78.

962 Stocker, R., 2011. Reverse and flick: Hybrid locomotion in bacteria. Proceedings of the National  
963 Academy of Sciences. 108, 2635-2636.

964 Stocker, R., 2011. Reverse and flick: Hybrid locomotion in bacteria. Proc Natl Acad Sci U S A.  
965 108, 2635-2636.

966 Swedlow, J.R., 2013. Quantitative fluorescence microscopy and image deconvolution. Methods  
967 Cell Biol. 114, 407-426.

968 Tahara, Y., Yamazaki, M., Sukigara, H., Motohashi, H., Sasaki, H., Miyakawa, H., Haraguchi,  
969 A., Ikeda, Y., Fukuda, S., Shibata, S., 2018. Gut Microbiota-Derived Short Chain Fatty Acids  
970 Induce Circadian Clock Entrainment in Mouse Peripheral Tissue. Scientific Reports. 8.

971 Taute, K.M., Gude, S., Tans, S.J., Shimizu, T.S., 2015. High-throughput 3D tracking of bacteria  
972 on a standard phase contrast microscope. Nature Communications. 6.

973 Turner, L., Ping, L., Neubauer, M., Berg, H.C., 2016. Visualizing Flagella while Tracking  
974 Bacteria. Biophysical Journal. 111, 630-639.

975 Wainwright, M., Phoenix, D.A., Marland, J., Wareing, D.R., Bolton, F.J., 1997. In-vitro  
976 photobactericidal activity of aminoacridines. J Antimicrob Chemother. 40, 587-589.

977 Wang, A., Dimiduk, T.G., Fung, J., Razavi, S., Kretzschmar, I., Chaudhary, K., Manoharan,  
978 V.N., 2014. Using the discrete dipole approximation and holographic microscopy to measure  
979 rotational dynamics of non-spherical colloidal particles. Journal of Quantitative Spectroscopy  
980 and Radiative Transfer. 146, 499-509.

981 Wang, A., Garmann, R.F., Manoharan, V.N., 2016. Tracking E-coli runs and tumbles with  
982 scattering solutions and digital holographic microscopy. Optics Express. 24, 23719-23725.

983 Wang, H., Lyu, M., Situ, G., 2018. eHoloNet: a learning-based end-to-end approach for in-line  
984 digital holographic reconstruction. *Optics express*. 26, 22603-22614.

985 Waterbury, J.B., Willey, J.M., Franks, D.G., Valois, F.W., Watson, S.W., 1985. A  
986 cyanobacterium capable of swimming motility. *Science*. 230, 74-76.

987 Waters, J.C., Wittmann, T., 2014. Chapter 1 - Concepts in quantitative fluorescence microscopy.  
988 In: J. C. Waters, T. Wittman (Eds.), *Methods in Cell Biology*, Vol. 123, Academic Press, pp. 1-  
989 18.

990 Wilson, L.G., Martinez, V.A., Schwarz-Linek, J., Tailleur, J., Bryant, G., Pusey, P.N., Poon,  
991 W.C., 2011. Differential dynamic microscopy of bacterial motility. *Phys Rev Lett*. 106, 018101.

992 Wyatt, P.J., 1970. Cell wall thickness, size distribution, refractive index ratio and dry weight  
993 content of living bacteria (*Staphylococcus aureus*). *Nature*. 226, 277-279.

994 Xiao, Y., Jisoo, H., Changgeng, L., Myung, K.K., 2014. Review of digital holographic  
995 microscopy for three-dimensional profiling and tracking. *Optical Engineering*. 53, 112306.

996 Xie, J., Khan, S., Shah, M., 2008. Automatic Tracking of *Escherichia Coli* Bacteria. In: D.  
997 Metaxas, L. Axel, G. Fichtinger, G. Székely (Eds.), *Medical Image Computing and Computer-  
998 Assisted Intervention – MICCAI 2008*, Springer Berlin Heidelberg, Berlin, Heidelberg, pp. 824-  
999 832.

1000 Yang, T., Zheng, T., Shang, Z., Wang, X., Lv, X., Yuan, J., Zeng, S., 2015. Rapid imaging of  
1001 large tissues using high-resolution stage-scanning microscopy. *Biomed Opt Express*. 6, 1867-  
1002 1875.

1003 Yuan, K., Jurado-Sánchez, B., Escarpa, A., 2021. Dual-Propelled Lanbiotic Based Janus  
1004 Micromotors for Selective Inactivation of Bacterial Biofilms. *Angewandte Chemie International*  
1005 Edition. 60, 4915-4924.

1006 Zhang, H., Stangner, T., Wiklund, K., Rodriguez, A., Andersson, M., 2017. UmUTracker: A  
1007 versatile MATLAB program for automated particle tracking of 2D light microscopy or 3D  
1008 digital holography data. *Computer Physics Communications*. 219, 390-399.

1009 Zhang, J., Zuo, C., Sun, J., Feng, S., Zhang, L., Fan, Y., Hu, Y., Kong, F., Chen, Q., Zhang, Y.,  
1010 Chen, D., Tao, T., Lin, F., Yang, Y., Tian, C., 2015. Software design of a digital holographic  
1011 microscope based on MFC, multi-document and multi-thread.

1012 Zhang, Y., Pedrini, G., Osten, W., Tiziani, H.J., 2003. Whole optical wave field reconstruction  
1013 from double or multi in-line holograms by phase retrieval algorithm. *Optics Express*. 11, 3234-  
1014 3241.

1015 Zhang, Y.-G., Wu, S., Xia, Y., Sun, J., 2014. *Salmonella* -infected crypt-derived intestinal  
1016 organoid culture system for host-bacterial interactions. *Physiological Reports*. 2, e12147.

1017 Zhu, T., Guo, Y., Zhang, Y., Lu, Z., Lin, X., Fang, L., Wu, J., Dai, Q., 2022. Noise-robust phase-  
1018 space deconvolution for light-field microscopy. *J Biomed Opt*. 27.

1019 Ziegler, A., Schock-Kusch, D., Bopp, D., Dounia, S., Radle, M., Stahl, U., 2015. Single bacteria  
1020 movement tracking by online microscopy--a proof of concept study. *PLoS One*. 10, e0122531.

1021

1022 See Supplemental Material at [*URL will be inserted by publisher*] for video animations of Fig. 8  
1023 (a) and Fig. 9 (a), (b).